ENERGY TRANSFER AND PHOTOSYNTHETIC LIGHT HARVESTING

GREGORY D. SCHOLES

Lash Miller Chemical Laboratories, University of Toronto, Toronto, Canada M5S 3H6

GRAHAM R. FLEMING[†]

Department of Chemistry, University of California, Berkeley; and Physical Biosciences Division, Lawrence Berkeley National Laboratory, Berkeley, California 94720-1460, USA

CONTENTS

[†]We dedicate this chapter to Stuart Rice, who has provided inspiration and friendship that have enriched our lives and careers.

Adventures in Chemical Physics: A Special Volume in Advances in Chemical Physics, Volume 132, edited by R. Stephen Berry and Joshua Jortner. Series editor Stuart A. Rice

I. INTRODUCTION

The collection of solar energy by photosynthetic plants, algae, and bacteria and the subsequent transfer of that energy to reaction centers is known as *light harvesting*. The pigment–protein complexes responsible for light harvesting are often collectively referred to as antennae [1–4]. Despite the variety of structures and diversity of pigment cofactors used through the plant and bacterial kingdoms, light harvesting is universally almost 100% efficient at low light levels. A further ubiquitous feature is the implementation of protective mechanisms to guard against damage that would result from singlet oxygen sensitization. One obvious key to the efficacy of light-harvesting antennae, which have large spatial cross sections for light absorption, is to ensure that the elementary energy transfer processes that transport excitation to the reaction center (RC) are ultrafast. For example, typically there are about 200 (bacterio)chlorophyll pigments associated with each reaction center. Then, if energy simply hops randomly from pigment to pigment until reaching the RC trap, we can estimate that on average $(0.72 \times 200 \log 200 + 0.26 \times 200) = 363$ hops are required prior to trapping. Given the fluorescence lifetime of (bacterio)chlorophyll, this simple picture tells us that the average time for each hop must be $< \tau_{\text{flu}}/(9 \times 363) \approx 300$ fs in order to achieve a quantum yield of excitation trapping greater than 90%. Thus over the past years there has been a happy conjunction between femtosecond spectroscopy and high-resolution structural models [2, 5, 6] which has enabled some systems—in particular the peripheral light harvesting antenna (LH2) [7–11] and the RC of purple bacteria [12–17] and Photosystem I of cyanobacteria and green plants [6] to be modeled at a reasonable level of sophistication. Likewise, the availability of detailed

structural and dynamical information has spurred the development of improved methods for calculating molecular interactions and energy transfer mechanisms.

To survey in detail the current state of knowledge of photosynthetic light harvesting would require an encyclopedic article. In this article we focus on the general principles that have been learned from studies of the purple bacterial and cyanobacterial systems. We discuss briefly the implications for green plant photosystems. We conclude with a discussion of questions that highlight areas that we feel are currently in need of investigation or resolution.

II. DYNAMICS OF ENERGY TRANSFER IN PHOTOSYNTHESIS

A. Structure and Dynamics

Light-harvesting pigment–protein complexes are employed by photosynthetic organisms to increase the spatial and spectral cross section per RC for collection of solar energy. In Fig. 1, we show structures of the peripheral light-harvesting complex LH2 of *Rps. acidophila* determined from X-ray crystallography [18]. In Fig. 2 we show the structure of the core light-harvesting complex LH1 of *Rps. rubrum* measured by low-resolution electron diffraction and a model based on the LH2 structure [19]. Recent studies have shown that LH1 may not always form a closed ring and may exist in a dimeric form. Figure 3 captures the layout of the antenna in purple bacteria, but should not be taken as a detailed model of the morphology of the entire photosynthetic unit. When grown under low light conditions the entire system contains about 250 bacteriochlorophyll (BChl) molecules RC. A stoichiometry of one LH1 per RC has been noted, the remaining BChl being contained in multiple LH2 complexes.

The structure of LH2 is known to 2.5 Å and 2.4 Å for *Rps. Acidophila* [18, 20] *and Rs. molischianum* [21, 22], respectively. The *Rps. acidophila* structure is based on subunits consisting of two trans-membrane α-helices (labeled α and β), which are arranged in a highly symmetric ring motif (C_9 symmetry in *Rps. acidophila* and C_8 symmetry in *Rps. molischianum*). This antenna complex contains a number of bound cofactors: two distinct rings of BChl *a* pigments, labeled B800 and B850, and at least one carotenoid per subunit, which makes a close approach to chromophores from each of these rings. In *Rps. acidophila* the B800 ring contains nine BChl *a* molecules while the B850 ring contains 18 BChl *a*. In *Rps. molischianum* the symmetry is eightfold, so the number of BChls is correspondingly reduced to 24 in total. LH1 is believed to be very similar in structure to LH2, but lacks an equivalent of the B800 ring, containing of single ring of 32 BChl *a* molecules known as B870 or B875 [23].

The overall timescale for trapping an excitation in the reaction center (and thereby initiating charge separation from the special pair) is 50–60 ps. The slowest step in this process is the final step from LH1 to the RC which takes

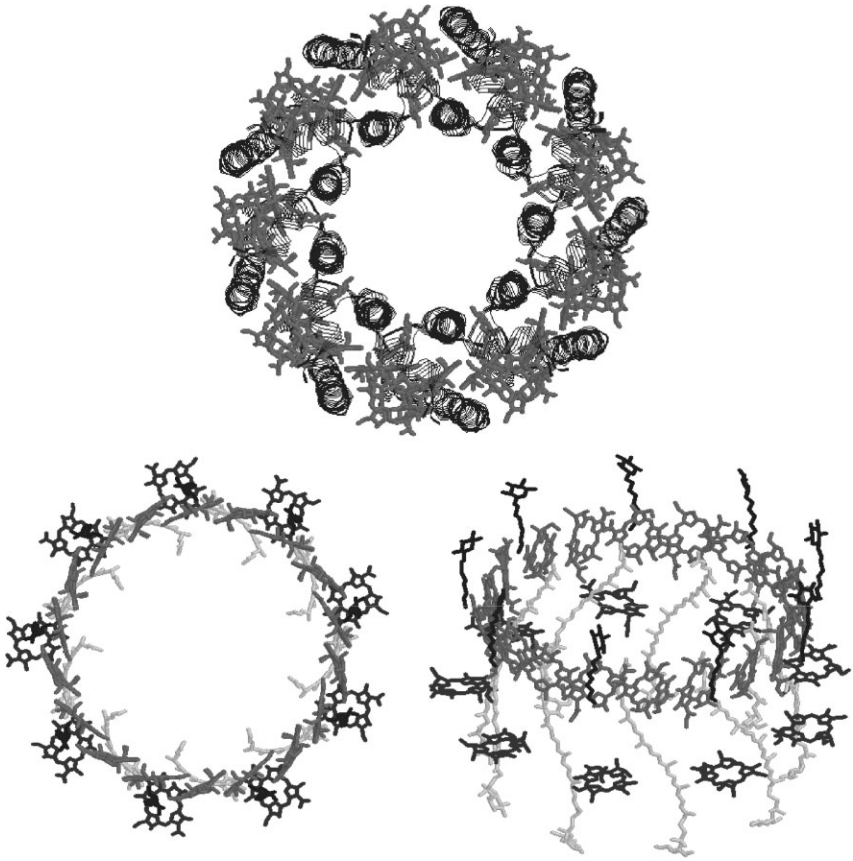

Figure 1. Illustration of the structure of the peripheral light-harvesting complex LH2 of the purple bacterium *Rps. acidiphila* strain 10050 [18]. The top view with α-helices represented as ribbons is shown at the top of the figure. The same view, but without the protein, leaving just the bacteriochlorophyll and carotenoid pigments, is shown at the lower left. On the lower right, this structure is shown tilted on its side, revealing the upper B850 ring of 18 Bchl pigments, the lower B800 ring of 9 Bchl pigments, and the carotenoids that weave their way between these rings. See color insert.

about 35 ps [24–26]. Transfer between LH2 complexes and from LH2 to LH1 takes 1.5–5 ps [27–29] and the transfers within each complex are much faster. For example, the transfer time between B800 and B850 in LH2 is about 700 fs at room temperature, [10, 30–35] while transfer between B800 molecules occurs on an average time scale of about 500 fs [35–38]. The dynamical time scale associated with the excited states in B850 and B875 is around 100 fs [39, 40], although the close proximity and strong electronic coupling (*vide infra*) of the

Figure 2. An illustration of the proposed structure of the LH1 ring of purple bacteria based on the LH2 structure [19, 22]. The protein has been removed from part of the ring to expose the B875 Bchl pigments and the carotenoids.

monomers comprising B850 and B875 make it far from clear that this process can be thought of as simple ''hopping'' of excitation between sites. Before attempting to provide a detailed picture of the energy transfer with B850 and B875, we need to understand the complex interplay between electronic coupling, electron–phonon coupling, and disorder.

The carotenoid molecules play dual roles as both light-harvesting and photoprotective pigments. We will briefly address the photoprotective role in Section VII.B. The overall efficiency of light harvesting from carotenoids (Cars) varies substantially from species to species [39–42]. In *Rb. sphaeroides* more than 95% of the photons absorbed by the Cars are transferred as excitation energy to the RC, while in strain 7050 of *Rps. acidophila* the overall efficiency is about 70%. Two electronic states of the Cars are involved in the energy transfer to the BChls. Energy transfer from the S_2 state of the Car is extremely rapid (50–100 fs) in all species studied so far, whereas the Car S_1 to BChl energy transfer time scale varies from $\sim$3 ps in *Rb. sphaeroides* to $>$25 ps and occurring with negligible quantum yield in *Rps. acidophila*.

Energy transfer processes have also been observed within the RC of purple bacteria [43–54]. The RC has 10 cofactors bound in a twofold symmetric arrangement: two closely spaced BChl *a* molecules (P_L and P_M) that comprise

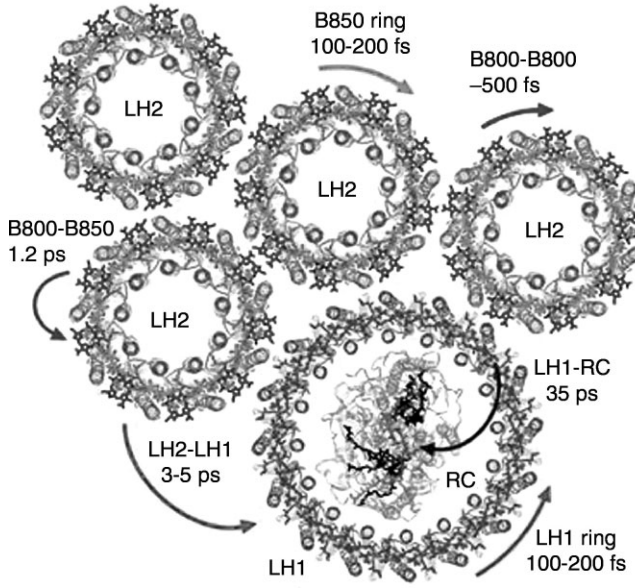

Figure 3. A schematic picture of the light-harvesting funnel in purple bacteria (*left*) and an illustration of how this corresponds to the layout of pigment–protein complexes (*right*). The approximate time scales of the various energy transfer processes are indicated.

the special pair or primary electron donor, two monomeric ''accessory'' BChl *a* molecules (B_L and B_M), two bacteriopheophytins (H_L and H_M), two ubiquinones (Q_A and Q_B), a carotenoid, and a nonheme iron as shown in Fig. 4 [55–58]. As early as 1972, Slooten [59] proposed that electronic energy transfer occurs from H and B to P in the *Rb. sphaeroides* RC. In the mid-1980s, ultrafast spectroscopy demonstrated that B to P energy transfer occurred in about 100 fs at both 300 and 10 K [43, 44]. More recently, it was shown that the appearance of P following excitation of H was 50% slower, than when B was excited directly, suggesting that B is a real intermediate in the H to P transfer process.

Many of the time scales described above have proven difficult, or impossible to obtain, using the standard Förster model [3, 60–64] of resonance energy transfer (coupling between point dipoles in donor and acceptor, overlap of measured donor emission spectrum with acceptor absorption spectrum, separation distance and mutual orientations specifiable by a simple parameter). Examples of processes where conventional calculations do not agree well with experiment are Car S_1 to BChl Q_y (the calculated rate would be zero!), B800 to B850 in LH2, and B to P in the RC, where calculated rates are always significantly

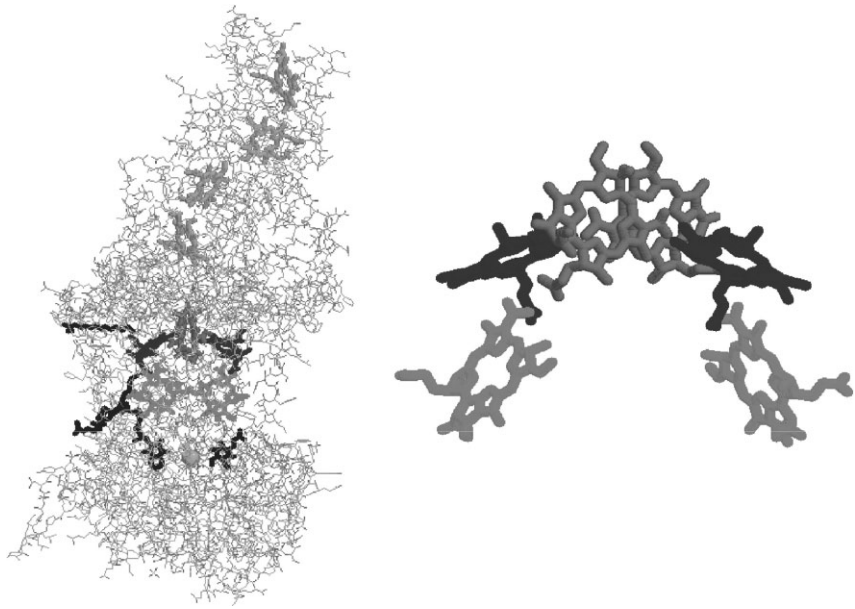

Figure 4. *Left*: Structural model of the photosynthetic reaction center of *Rps. viridis* from crystal structure data. *Right*: Arrangement of the special pair (dark gray), accessory bacteriochlorophyll (black), and the bacteriopheophytin (light gray) pigments.

slower than their measured values. In addition, the temperature dependence of these later two processes is strikingly weak and not predicted by simple calculations. Such discrepancies between theory and experiment have led to much speculation that new mechanisms are required to understand photosynthetic energy transfer. In this review, we will attempt to show that each of ''troublesome'' processes described above can be explained quantitatively by generalizing the conventional Förster description to include the effects of (a) multiple donors and acceptors, possibly with strong coupling between members of each group, (b) closely spaced donors and acceptors, and (c) energetic disorder among the donors and acceptors. We find that very weak or even normally forbidden transitions in a molecular aggregate may participate in efficient energy transfer via the Coulombic coupling mechanism, rather than by orbital overlap (e.g., the exchange or Dexter mechanism) [4] as it is often supposed. The remarkable efficiency of energy transfer in photosynthetic pigment–protein complexes of both plants and bacteria seems likely to be understandable in this context. A primary implication of our work is that optical spectroscopy is limited as a tool to determine electronic couplings in molecular aggregates. This means that, at the present time, general design principles for

light-harvesting structures can only be revealed by a combination of experiment and theory.

More complex dynamics underlie the energy transfer processes that have been observed within the B850 and B875 rings of LH2 and LH1. In this case, an excitonic theory is required in order to relate linear and nonlinear spectroscopic observables to the underlying dynamics. Finally, in the case of Photosystem I from a cyanobacterium, both weak and strong coupling cases exist within the set of 96 nonequivalent Chls comprising the core antenna/RC complex.

B. Spectra of Purple Bacterial LH Complexes

Before turning to a description of electronic coupling in the LH complexes of purple bacteria, it is appropriate to review briefly the mechanisms used in the natural system to shift the absorption frequencies of the various components, such as B800, B850, and so on (Fig. 5).

In relative isolation the BChl-*a* molecules absorb at 772 nm (the Q_y band), 575 nm (the Q_x band), and 360 and 390 nm (the B bands). The carotenoids have a strong $S_0 \rightarrow S_2$ absorption in the region 450–550 nm, while their $S_0 \rightarrow S_1$ transition is dipole-forbidden and it is not found in the one-photon absorption spectrum.

However, each of these states plays a role in gathering light. The operation of the light-harvesting antenna of purple bacteria is based on an energy funnel to focus excitation energy to the reaction center. There are two obvious ways to construct such a funnel: (1) Select different chemical species that absorb at the

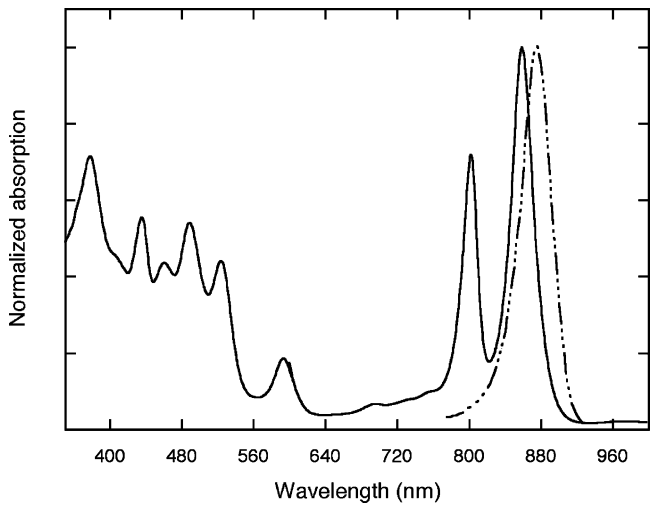

Figure 5. The absorption spectra of LH2 of *Rps. acidophila* (solid line) and LH1 (dash–dotted line).

required wavelength or (2) use exciton (and solvation) interactions to progressively red shift the spectra of the same chemical species. In purple bacteria, nature has adopted the second strategy for the BChl components: They use both interactions between the pigments (''excitonic coupling'') and interactions between individual pigments, along with the protein environment to modify the spectroscopy of antenna components. In LH2, the BChl *a* absorption bands are located at 800 nm (B800) and at 850 nm (B850), while in LH1 the BChl *a* absorption has a maximum at 875 nm (B875). The B800 molecules interact weakly with each other and with the B850 molecules. In contrast, the B850 and B875 molecules are fairly strongly coupled amongst themselves to produce at least a significant portion of the red shift. However, the role of the protein is also evident here, as demonstrated by Fowler et al., who showed that site specific mutants of LH2 that removed specific hydrogen-bond interactions between the protein and the B850 chromophores, produced significant blue shifts of the absorption band [65–67]. One of the most intriguing questions in the study of light harvesting is whether there is an intrinsic advantage to the excitonic coupling strategy, which necessarily brings with it some degree of delocalization of the electronic states. In many other systems, chemical modification is also used to expand spectral coverage. For example, the binding of both chlorophyll *a* and chlorophyll *b* in LHC II [2].

The carotenoid constituents of the antenna systems also expand the spectral coverage of the antenna, although the efficiency of carotenoid to chlorophyll transfer varies significantly between species. The strongly allowed S_0–S_2 transition of carotenoid in the 450- to 550-nm spectral region significantly enhances absorption in this wavelength range and can transfer excitation to BChl or Chl molecules via the conventional Coulombic coupling mechanism. However, upper excited states are very short lived and rapid internal conversion to the S_1 state will occur in parallel with the energy transfer. The efficiency of S_1 to BChl or Chl energy transfer seems to vary significantly from complex to complex and species to species.

In addition to the systematic variations in transition frequencies of specific classes of pigments such as B800 or B850, there is significant disorder in the excitation energies from site to site and from complex to complex [10, 68–71]. This distribution of monomer energies can arise from (a) side-chain disorder in the protein, (b) deformation of the BChl macrocycle, (c) binding of ions, (d) ionizable side chains being near their pK_a values and thus existing in both neutral and ionized forms, (d) local or global distortions of the structure, and (e) the limited statistical sampling of full distribution of site energies possible in a complex of, for example, 9 or 18 monomer units. In addition to these types of disorder (generally referred to as *diagonal disorder*) in the excitonically coupled systems, variations in the electronic coupling between monomers (*off-diagonal disorder*) can also occur [72].

The fundamental question arising from the structure–function–dynamics relationships within a light-harvesting antenna is simply stated: What is the mechanism by which excitation moves in the antenna, and why is the overall process so wonderfully efficient? In this review we explore our knowledge of the ingredients required to formulate an answer to this question. We will describe our present understanding of the electronic interactions between the pigments, the line-broadening processes arising from electron–phonon coupling and disorder, and the implications of multiple, closely spaced chromophores for the dynamics. Finally, we will attempt to describe how the interplay between all these phenomena determines the dynamics of light-harvesting and funneling.

III. ELECTRONIC COUPLING AMONG THE CHROMOPHORES

A. Preface

When Förster [60] initially formulated his theory of energy transfer via the inductive resonance mechanism, he considered the interaction of single pairs of chromophores spaced by distances that are large compared to the size of the molecules. The situation in light-harvesting complexes is often rather different: Molecules are spaced by distances that are small compared to the overall molecular dimensions, making the definition of donor–acceptor separation and relative orientation ambiguous at best. In addition, there are often several or even many donor and acceptor molecules in close proximity, and these interactions may perturb the monomer spectral line-shape significantly. As we will describe in detail below, if any of the electronic couplings are strong enough to perturb significantly the spectral line shape or radiative rates, the standard Förster formulation of energy transfer becomes inadequate. An important example of this effect is the strong interaction between the two BChls of the special pair of the purple bacterial reaction center, which alter and shift the absorption spectrum dramatically compared to that of the monomer.

When the energy transfer involves one forbidden transition, it has been conventional to invoke mechanisms of electronic interaction other than Coulombic coupling, such as electron exchange via orbital overlap as originally formulated by Dexter [4]. Here an important general issue arises which relates to the length scale on which the molecular transition density is characterized by optical spectroscopy. In essence, the photon characterizes the molecular transition density in the far field, thus averaging over the entire molecular dimension. In the confined geometry of molecular aggregates, such as light-harvesting complexes, neighboring molecules may sense the shape of each other's transition density on a much finer scale [73]. It is clear that this effect will produce quantitative errors if the transition densities are approximated as

point dipoles, but it is perhaps less obvious that qualitative mechanistic errors can arise if forbidden transitions are assumed to be incapable of Coulombic coupling to allowed transitions of molecules separated by distances smaller than the overall donor molecular dimensions. This type of symmetry breaking is important in, for example, the S_1 to Q_y transitions of carotenoids to BChls, and we will describe it in detail below. Both qualitative and quantitative aspects of this issue can be handled by explicitly calculating the Coulombic interaction between the transition densities of donor and acceptor, but now these must be obtained from electronic structure calculations, thus breaking the reliance on only experimentally determined quantities, which is the great strength of the Förster theory.

Our *ab initio* quantum chemical study of electronic interactions in LH2 [74] provides a starting point for the discussion. The calculated highest occupied molecular orbital (HOMO) for the intrapolypeptide BChl dimer in LH2 is shown in Fig. 6. It was anticipated that there would be significant orbital overlap between these two BChls, and this may assist delocalization of energy about the B850 ring. The calculated overlap density between the monomer BChl HOMOs is shown also in Fig. 6. The corresponding overlap integral was determined to be 1.72×10^{-3} (HF/3-21G*). Is overlap of this magnitude between two BChls significant for calculations of EET? According to a simple analysis based on the calculated overlap, it is not, unless the closest approach of the BChls is 3 Å or less. Note that there is only overlap between one of the four pyrrole rings of each macrocycle. If the BChl molecules were to be arranged in a more sandwich-like geometry, rather than being offset as in LH2, this overlap would increase owing to more orbital density being able to overlap. We can model this only by considering the distance-dependence of the overlap with respect to the spatial distribution of orbital density on each molecule. This is different from pushing the dimer together, which would increase the V^{short} coupling according to a simple exponential distance-dependence. Doubling the overlap would quadruple V^{short}, consequently having a significant effect of the EET rate at larger separations.

We have quantified the orbital overlap-dependent coupling for the BChl dimers in the B850 ring of LH2 [74]. Nonetheless, at closest approach separations of 4 Å or more, it seems reasonable to ignore the V^{short} contribution to the coupling. However, we have found that at typical interchromophore separations identified in light-harvesting complexes, the dipole approximation is unreliable for quantifying the Coulombic interactions. The dipole approximation completely ignores the shape of the interacting molecules—which turns out to be important in many cases. To overcome this barrier, we have developed the transition density cube method for calculating Coulombic interactions between electronic transitions, as we describe below. In addition, in multichromophoric systems, use of the dipole approximation can mask the way that energy transfer

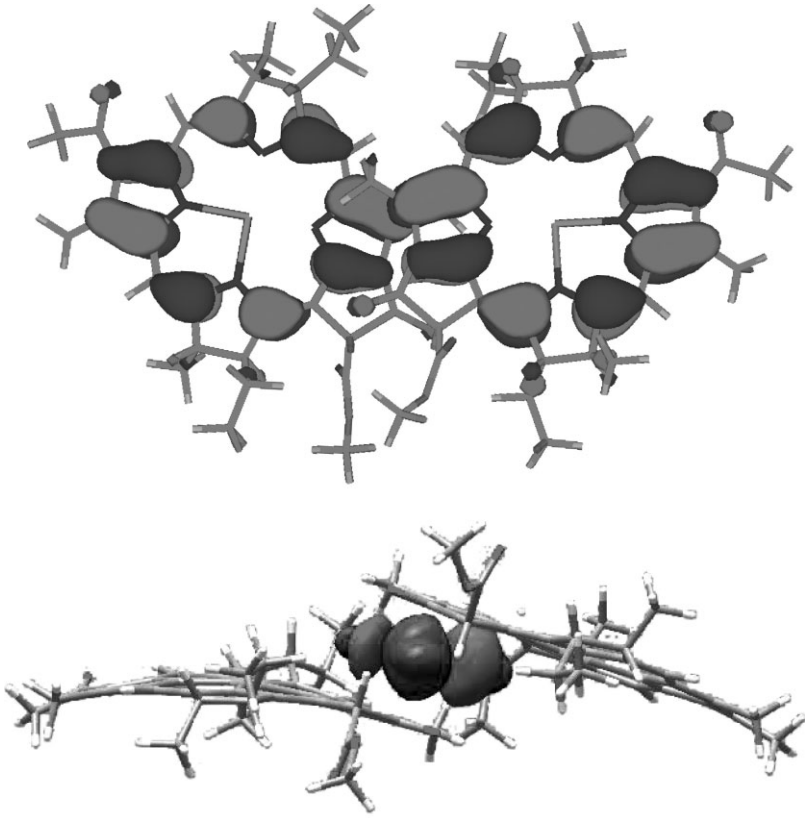

Figure 6. *Top*: A HOMO calculated for a B850 dimer of LH2 (HF/3-21G*). *Bottom*: The overlap density between the two Bchl chromophores is plotted.

dynamics are dictated by the arrangement of molecules in an aggregate. This latter point is rather subtle, and we will describe it further by way of the theory and examples in Section VI.

B. The Transition Density Cube Method

It is straightforward to show [75] that the Coulombic interaction that promotes excitation transfer between two two-level systems is given by the integral

$$\begin{aligned} V^{\mathrm{Coul}} &= 2\int \mathrm{d}\tau\; d'(1)a(2)r_{12}^{-1}d(1)a'(2) \\ &\equiv 2(d'd \mid aa') \end{aligned} \tag{1}$$

where d (d') is the HOMO (LUMO) of the donor, etc. d and a are doubly occupied in the ground state, while the excited state is represented as a single excitation from the ground state.

We have found it useful to express this Coulombic interaction in terms of transition densities (TDs) [73]. It has thereby been possible to calculate quite accurately, and with moderate computational effort, Coulombic interactions and energy transfer dynamics in rather complex light-harvesting assemblies. Furthermore, we have thus been able to gather several new physical insights into the mechanism of light harvesting. For example, we will describe here the physical, as well as practical, meaning of the dipole approximation with respect to energy transfer. We will show how and why the shape of molecules is just as important as their separation and orientation. Finally, we will show that the degree to which a transition is allowed or forbidden does not necessarily have direct implications for light-harvesting efficiency.

In general, the Coulombic interaction can be written in terms of the two-particle spinless transition density $\Pi_{KL,RS}$ that connects the states K and L on the donor (D) and connects the states R and S on the acceptor (A):

$$V^{\text{Coul}} = \frac{e^2}{4\pi\varepsilon_0} \int \frac{\Pi_{KL,RS}(\mathbf{r}_1, \mathbf{r}_2)}{|\mathbf{r}_1 - \mathbf{r}_2|} \, \mathrm{d}\mathbf{r}_1 \mathrm{d}\mathbf{r}_2 \tag{2}$$

Usually two-particle densities can only be written in terms of one-particle densities for single-configuration wavefunctions. However, because electron 1 and states K and L are localized on molecule D, whereas electron 2 and states R and S are localized on A, it is possible to factorize $\Pi_{KL,RS}(\mathbf{r}_1, \mathbf{r}_2)$ when nonorthogonality effects resulting from interpenetration of donor and acceptor electron densities are negligible. Thus we obtain:

$$V^{\text{Coul}} = \frac{e^2}{4\pi\varepsilon_0} \int \frac{P^D_{KL}(\mathbf{r}_1) P^A_{RS}(\mathbf{r}_2)}{|\mathbf{r}_1 - \mathbf{r}_2|} \, \mathrm{d}\mathbf{r}_1 \mathrm{d}\mathbf{r}_2 \tag{3}$$

The single-particle transition density matrix connecting states K and L of molecule D is defined as usual [76]:

$$P^M_{KL}(\mathbf{r}_1) = N \int \Psi_K(\mathbf{x}_1, \mathbf{x}_2, \ldots, \mathbf{x}_N) \Psi^*_L(\mathbf{x}'_1, \mathbf{x}'_2, \ldots, \mathbf{x}'_N) \mathrm{d}\mathbf{x}_2 \ldots \mathrm{d}\mathbf{x}_N \mathrm{d}\mathbf{x}'_2 \ldots \mathrm{d}\mathbf{x}'_N \mathrm{d}s_1 \tag{4}$$

where N is a normalization constant, $\mathbf{x}_i$ are the spatial and spin coordinates of electron i, and s_1 is the spin of electron 1.

Owing to the orthogonality between states K and L, $P_{KL}(\mathbf{r}_1)$ integrates to zero. Physically, this is because no net charge is gained or lost during an

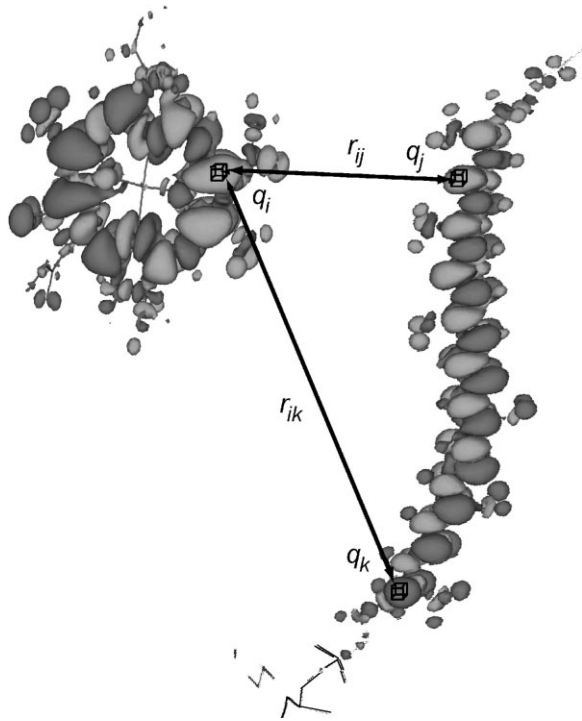

Figure 7. Transition densities calculated for a Bchl molecule and a carotenoid. Density elements, containing charge q_i, q_j, and so on, are depicted together with their corresponding separation r_{ij}. Summing the Coulombic interaction between all such elements gives the total Coulombic interaction, which, according to the TDC method, promotes energy transfer. See color insert.

electronic transition. A plot of the transition density, as shown in Fig. 7, reveals the manner in which the electron density of molecule D is polarized by interaction with light, in such a way as to induce a transition from L to K.

Since the wavelength of light is typically much larger than the physical size of a molecule, in optical spectroscopy it is usual to condense the information in the transition density of an allowed transition to its dipole moment,

$$\mu_{\alpha}^{LK} = \int (r_{\alpha})_1 P_{KL}^{M}(\mathbf{r}_1)\, \mathrm{d}\mathbf{r}_1, \tag{5}$$

where the index α denotes the x, y, and z components of the vector. It is this quantity μ_{α}^{LK} that determines the strength of electric dipole-allowed electronic transitions between states L and K according to the dipole approximation.

Similarly, if we assume that the donor and acceptor electronic transitions are electric dipole-allowed, and the condition $|\mathbf{r}_1 - \mathbf{r}_2| \gg$ the spatial extent of D and A is satisfied, then Eq. (3) can be written in terms of transition multipoles (dipole, quadrupole, etc.) and a corresponding power series in $1/R$, where R is the center-to-center separation of the molecules [4, 75, 77]. Förster was the first to propose a connection between electronic spectra and the electronic coupling based on these arguments, so this is the approximation normally used in conjunction with Förster theory [60]. We note that this dipole approximation in the Coulombic coupling is a different kind of dipole approximation than that relating to the interaction between a molecule and light [77–80].

When the donor and acceptor molecules are nearby to each other, as is typically the arrangement in photosynthetic light-harvesting antenna complexes, the shape of the transition densities is very important in determining the electronic coupling. In that case, the correct physical picture is lost when the shape information in the transition density is averaged away by applying the dipole approximation. This idea was recognized by London in connection to van der Waals forces [81]:

> ... it is clear that even the dipole terms of this power series must turn out to be quite inappropriate if one has to consider oscillators of some length extended over a large region of a chain molecule. Another molecule would interact chiefly with one end of such a long virtual oscillator, and this situation would be completely distorted if one were to represent the oscillator by a decomposition into point-form multipoles, all located in the center of the molecule. It would obviously be much more appropriate in this case to represent each oscillator by several distinct poles, ''monopoles,'' of different sign, suitably located in the molecule, thus directly taking account of the actual extension of the oscillator in question.

This idea is illustrated in Fig. 7, where we show the calculated (CI-singles/3-21G*) transition densities for the BChl-*a* Q_y transition and the Car (rhodopin glucoside) S_2 transition. The Coulombic interaction between these transition densities is the sum over all the interactions between charge ''cells'' on each transition density matrix, $q_i q_j / r_{ij}$. From inspection of this figure, it is evident that the topology of the transition densities cannot be ignored—for instance, r_{ij} is significantly different from r_{ik}. The only time that it is useful to calculate the interaction from mulipole moments of the transition densities and one average donor–acceptor separation is when the two molecules are sufficiently far apart that all the r_{ij} are similar. We suggest that a useful rule of thumb is to check whether or not the value of R is insensitive to the exact positions on the donor and acceptor molecules that are deemed to be the molecular centers. This will indicate that a multipolar expansion of the interaction potential provides a useful route to evaluation of Eq. (3).

We conclude that when the donor and acceptor molecules are closely located relative to molecular dimensions, the analogy between synergistic absorption and emission processes and the V^{Coul} interaction breaks down. We now need to think about V^{Coul} in terms of ''local interactions'' between the donor and acceptor transition densities because there is a distinct and important difference between (a) averaging over wavefunctions and then coupling them [Eq. (6a)] and (b) averaging over the coupling between wavefunctions [Eq. (6b)].

$$\frac{\left|\sum_i q_i \vec{\mathbf{r}}_i\right| \left|\sum_j q_j \vec{\mathbf{r}}_j\right|}{R_{DA}^3} \tag{6a}$$

$$\sum_{i,j} \frac{q_i q_j}{r_{ij}} \tag{6b}$$

Here we consider discrete charges q_i at position r_i on donor molecule D and charges q_j at position r_j on acceptor A. $r_{ij} = r_i - r_j$ and R_{DA} is the center-to-center separation between D and A, and κ_{DA} is the orientation factor between transition moments $\vec{\mu}_{\mathrm{D}} = \sum_i q_i r_i$ and $\vec{\mu}_{\mathrm{A}} = \sum_j q_j r_j$.

The key is that a single-center expansion of the transition density, implicit in a multipolar expansion of the Coulombic interaction potential, cannot capture the complicated spatial patterns of phased electron density that arise because molecules have shape. The reason is obvious if one considers that, according to the LCAO method, the basis set for calculating molecular wavefunctions is the set of atomic orbital basis functions localized at atomic centers; a set of basis functions localized at one point in a molecule is unsatisfactory.

To execute Eq. (3) numerically, we have used *ab initio* quantum chemical methods to calculate *transition density cubes* (TDCs) for the donor and acceptor from CI-singles or time-dependent density functional theory wavefunctions. A TDC is simply a discretized transition density,

$$\tilde{P}_{KL}^{M}(x,y,z) = V_\delta \int_z^{z+\delta_z} \int_y^{y+\delta_y} \int_x^{x+\delta_x} P_{KL}^{M}(\mathbf{r}_1) \tag{7}$$

where the δ_α denote the grid size of the transition density cube and $V_\delta = \delta_x \delta_y \delta_z$ is the element volume. In the TDC method the donor and acceptor transition densities are each represented in a 3D grid. Charge density in each cell of the donor q_i is coupled with that in each cell of the acceptor q_j via,

$$V^{\mathrm{Coul}} \cong \sum_{i,j,k} \sum_{l,m,n} \frac{\tilde{P}_{KL}^{D}(i,j,k)\tilde{P}_{RS}^{A}(l,m,n)}{4\pi\varepsilon_0 \left|\mathbf{r}_{ijk} - \mathbf{r}_{lmn}\right|}. \tag{8}$$

Typically we use TDCs consisting of $\sim 10^6$ elements, each of volume ~ 0.23 bohr^3. The shape of a ''cube'' is chosen to contain best the shape of the molecule (it does not have to be a cube). Using Eq. (8), the donor–acceptor interaction topology is accounted for to a fine level of detail.

The accuracy of Eq. (8) is limited by the number of elements in the TDC, the size of each element, and the accuracy of the quantum chemical wavefunctions. A consequence of the first two factors is the problem of residual charge. That is, the sum of the charge over all cube elements is not zero, as it should be, but can be $\sim 0.01\ e$. This residual charge can significantly affect the calculated coupling because, reverting to the language of the multipole expansion, it provides spurious charge–charge and charge–dipole interactions between the transition densities. To compensate for this residual charge q_R in a TDC with N elements, we subtract a quantity q_R/N from each element in the TDC, such that the residual charge is reduced to $\sim 10^{-14}\ e$. Upon evaluating Eq. (8), one must also remove singularities that arise when cube elements of the donor TDC overlap with those of the acceptor TDC. We simply ignore these contributions to V^{Coul}, which is justified because the overlap density (i.e., the significance of overlapping transition density) must be small anyway when V^{Coul} dominates the electronic coupling.

A challenge for calculating the magnitude of electronic couplings accurately via the TDC method is to determine the ground- and excited-state wavefunctions as precisely as possible. However, this is generally an easier task than might be anticipated, for the reason that the most important result of the calculation is the shape of the TD. The shape of the TD is, of course, constrained by the shape of the molecule, and thus is easily obtained. Electronic couplings are overestimated by CI-singles TDCs, for the same reasons that transition dipole moments—for example, μ^{calc} from Eq. (5)—are overestimated. However, because the shape of the TD is well-calculated, it is possible to scale uniformly the TDC in such a way that Eq. (8) gives the experimental result for the transition dipole moment μ^{exp}. We do this by multiplying each element in the cube by $\mu^{\mathrm{exp}}/\mu^{\mathrm{calc}}$ (or equivalently post-processing the calculated coupling). This method does not work for forbidden transitions, of course. If TDs are calculated using time-dependent density functional theory or semiempirical methods like INDO [82], no scaling is necessary [83].

If wavefunctions are calculated using semiempirical methods that assume zero overlap between atomic orbitals (AOs) on different atomic centers, then a Mulliken population analysis [84, 85] can be applied to the calculated TD to yield transition monopoles distributed over each atomic center. Such an approach has proven to be effective [82] an advantage being that the interaction between distributed monopoles can be computed considerably faster then that between TDCs. At the same time, the basic topology of the donor–acceptor

interaction is preserved. Here we describe this method in more detail for the more general case wherein differential overlap is preserved.

A general TD calculated in terms of a CI expansion of molecular orbitals (MOs) may be transformed to an AO basis P_{ij}^{KL} in terms of $\{\chi_i(\mathbf{r})\}$ such that [76],

$$P_{KL}(\mathbf{r}) = \sum_{i,j} P_{ij}^{KL} \chi_i(\mathbf{r}) \chi_j(\mathbf{r}). \tag{9}$$

The TD can then be analyzed in terms of the normalized orbital and overlap densities

$$d_i(\mathbf{r}) = (\chi_i(\mathbf{r}))^2, \quad d_{ij}(\mathbf{r}) = \frac{\chi_i(\mathbf{r})\chi_j(\mathbf{r})}{S_{ij}}, \tag{10}$$

where $S_{ij} = \langle \chi_j | \chi_i \rangle$ and the associated transition charges are

$$q_i = P_{ii}^{KL}, \quad q_{ij} = 2S_{ij}P_{ij}^{KL}, \tag{11}$$

leading to

$$P_{KL}(\mathbf{r}) = \sum_i q_i d_i(\mathbf{r}) + \sum_{i<j} q_{ij} d_{ij}(\mathbf{r}). \tag{12}$$

By summing over the AOs localized at each atomic center and integrating these over $\mathbf{r}$, we can reduce Eq. (12) to a distribution of TD monopoles located at each atomic center, and a distribution of overlap-densities from the second term on the right-hand side of Eq. (12). When the overlap densities arise from overlap of AOs on different atomic centers, the resulting TD monopole can arbitrarily be placed halfway between the two atomic centers. More sophisticated reductions of Eq. (12) represent each TD monopole as a multipole expansion about the atomic center.

C. Coulombic Couplings in LH2

The availability of high-resolution structural data on various light-harvesting complexes has made it possible to relate spectroscopic observations of dynamics and their time scales to a detailed physical picture. An important link connecting the structural model to the dynamical information is the electronic Hamiltonian, containing the site transition energies for each chromophore and the electronic couplings between the chromophores. This information can be obtained from quantum chemical calculations, as has been described previously [9, 11, 13, 29, 74].

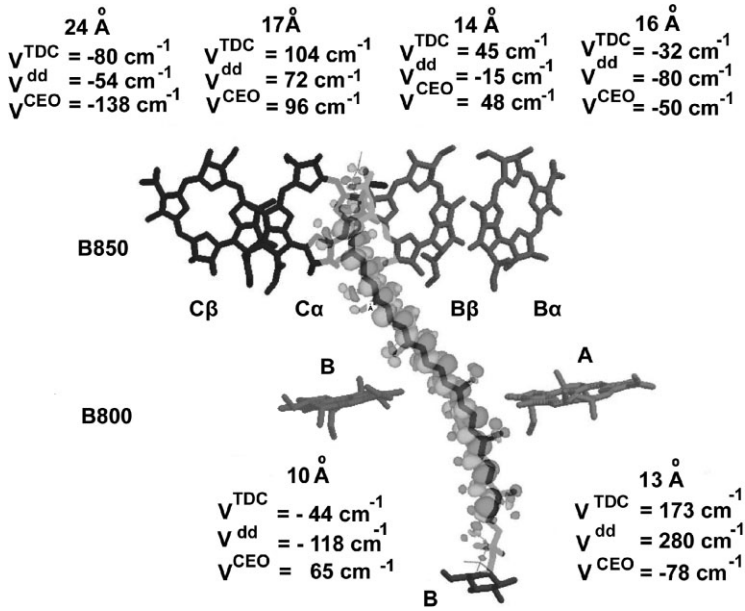

Figure 8. A summary of couplings calculated between the Bchl Q_y transition and the carotenoid S_2 transition for LH2. V^{TDC} are those calculated by the TDC method for *Rps. acidophila* [73], the V^{dd} provide a comparison with the dipole–dipole method, and V^{CEO} are those calculated for *Rs. molischianum* using the CEO method [11].

In Fig. 8 we depict part of the structure of LH2 from *Rps. acidophila* (strain 10050) showing four Bchls from the B850 ring and two from the B800 ring [18]. The associated rhodopin glucoside carotenoid threads its way past each of these rings. It is known that energy is transferred efficiently from the dipole-allowed S_2 state of the carotenoid to the Bchls—primarily via their Q_x states [21, 23, 25, 73]. Here we summarize electronic couplings we have calculated between the S_2 state of the rhodopin glucoside and the Q_x state of each Bchl for this complex using the TDC method, based on CIS/3-21G* wavefunctions, compared to electronic couplings estimated using the dipole approximation with respect to the same transition densities. It is immediately apparent that the dipole approximation will be problematic because it is not clear how best to define the interchomophore separations. We used the centers of each transition density, and we provide these distances in the figure. Quantitatively, we see that the results of the dipole approximation can, at best, be described as unpredictable compared to the TDC method and may not even predict correctly the sign of the coupling. This is because, for example, the Bchls in the B850 interact chiefly with just the top of the carotenoid transition density, but interact

comparatively little with its other end. Apparently, the electronic coupling is determined by the shape and position of the carotenoid and the Bchl, which in turn dictates how their transition densities interact.

In Fig. 8 we also provide electronic couplings reported by Tretiak et al. [11] for the LH2 of *Rs. molischianum*. These couplings were calculated using the collective electronic oscillators (CEO) method [86, 87]. Note that the B800-carotenoid couplings differ between the two species, owing to the 90° difference in orientation of the B800 Bchls.

D. Carotenoid S_1 State and Electronic Coupling

The mechanism of electronic coupling that promotes Car $S_1 \rightarrow$ BChl EET has generally been rather mysterious, and is usually discussed in light of the relative merits of Förster versus Dexter energy transfer theories. The conventional wisdom is that, because Förster theory cannot be applied when the donor or acceptor transition is optically forbidden, Car S_1 to BChl coupling must be mediated by Dexter EET—and hence be dictated by the degree of orbital overlap between donor and acceptor states. Our recent *ab initio* calculations of B850 couplings in LH2 evince the possibility that V^{short} contributions to the Car S_2 to BChl coupling could reasonably have magnitudes of between 1 and 10 cm^{-1} [74]. However, according to our previous analysis of the microscopic mechanisms operative in Car S_1 to BChl coupling, V^{short} is likely to be much smaller than for Car S_2 to BChl coupling [77].

Considering that the shape and arrangement of transition densities of donor and acceptor were found to be so important for the carotenoid S_2 state interacting with the Bchl transitions in LH2 [73], the overall symmetry of the electronic transition may not be as restricting as might be supposed from the optical spectroscopy. In other words, there could likely be a significant Coulombic coupling between the carotenoid S_1 state and the Bchl transitions in LH2. By reasoning that the transition densities are mostly determined by the shape of the molecules, Walla et al. [83] estimated the approximate rhodopin glucoside to B850 Bchl couplings by scaling the S_2 to Bchl couplings uniformly such that the modified Förster theory for molecular aggregates (see Section VI. B) predicted their measured S_2-B850 EET rates. Very soon after this, Hsu et al. calculated these couplings using the TDC method (based on TD-DFT methods) and found remarkable agreement [1]. These results are collected in Table I, where they are also compared to Tretiak et al.'s [11] results for *Rs. molischianum*, determined from CEO calculations.

Hsu et al. [1] investigated the origin of the substantial Coulombic coupling between the carotenoid S_1 state and Bchls in LH2. They found that a significant contribution could be attributed to mixing of the $2A_g$ and the B_u carotenoid states, induced by distortion of the carotenoid structure. However, even for a completely planar carotenoid molecule, with a forbidden $S_0 \rightarrow S_1$ transition, the

TABLE I
Calculated Electronic Couplings (cm^{-1}) Between the Carotenoid S_1 State and Bchl Q_y State in LH2

	$B800_A$	$B800_B$	$\alpha B850_B$	$\beta B850_B$	$\alpha B850_C$	$\beta B850_C$
[a]	26	−7	−5	7	16	−12
[b]	31	−10	−5	9	32	−18
[c]	39	−0.4	3	−4	−4	−41

[a]Estimated by scaling the rhodopin glucoside S_1–Bchl Q_y electronic couplings in LH2 of *Rps. acidophila* calculated by the TDC method [83].
[b]Calculated (*Rps. acidophila*) by the TDDFT method [161].
[c]Calculated (*Rs. molischianum*) by the CEO method [11].

couplings were still found to be significant. The transition densities calculated for the rhodopin glucoside S_1 and S_2 transitions are plotted in Fig. 9. It can be conjectured that the Coulombic interaction with, for example a B850 Bchl, will be reasonable favorable for each of these states, given that the Bchl interacts principally with just the top end of the molecule. On the other had, it is evident that, overall, the symmetry of the transition densities differ: The S_1 state has a

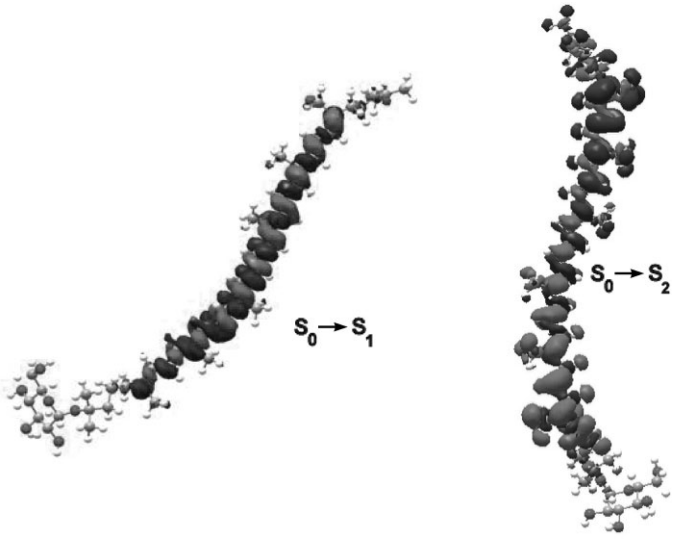

Figure 9. A comparison of transition densities for rhodopin glucoside calculated using TDDFT (6-31++g** basis set). On the right the $S_0 \rightarrow S_2$ transition is shown, with its large dipole transition moment being evidenced by the change in sign of this TD from one end of the molecule to the other. On the left the $S_0 \rightarrow S_1$ transition is shown. The symmetry of the TD causes the transition to be optically forbidden. See color insert.

symmetrically phased transition density relative to the middle of the backbone, whereas the S_2 state is antisymmetric and hence dipole-allowed.

E. Doublet States and Electronic Coupling

In isolated reaction centers, RCs, of photosynthetic purple bacteria, the primary electron donor P* can quench excitation by rapid EET from higher-energy RC pigments, either from the monomeric "accessory" bacteriochlorophyll-*a* molecules (B_L and B_M) or from the bacteriopheophytins (H_L and H_M). The photoexcited dimer P* then transfers an electron to H_L within three picoseconds with a quantum yield of nearly unity to form the radical dimer P^+ [88, 89]. If, however, the primary electron donor is oxidized (either chemically or under high light intensity) [90] to form P^+ before photoexcitation, electron transfer and thus photosynthesis are blocked. After excitation of B at 800 nm, the absorption of B recovers in ~130 fs in the neutral RC and in ~150 fs in the oxidized RC. In both cases, the ground-state recovery of B has been interpreted as energy transfer from B to P within the RC. Remarkably, EET to the oxidized primary electron donor (from the accessory bacteriochlorophyll or from the antenna) apparently still occurs [45, 46, 59, 91] even though the strong absorption band P has disappeared. Why the wild-type RC and oxidized RC primary electron donors are equally efficient quenchers of the excitation has been an unanswered question for the last 30 years. Recently, however, we have been able to explain this observation [17, 92].

We summarize below how we went about modeling EET in the neutral RC based on our model for EET in molecular aggregates. The most significant feature that differentiates the oxidized RC from the neutral reaction center, and any previously reported energy transfer systems we are aware of, is that the acceptor is a dimeric radical. Therefore, the focus of the problem was to determine the electronic energies and origins of the electronic transitions of the oxidized special pair acceptor and to quantify the electronic coupling between each of these relevant transitions and the donor transitions.

After recognizing that EET between a singlet state and a doublet state is spin-allowed, since no spin flips are necessary $({}^2({}^1B^*\ {}^2P^+) \rightarrow {}^2({}^1B^2P^{+*}))$, it was apparent that we could employ the TDC method to calculate the electronic coupling between B and P^+. Still, the acceptor states needed to be identified before calculating their transition densities. This was not a trivial problem, owing to (a) the complex internal spin structure in the P^+ electronic transitions and (b) the difficulty identifying the P^+ absorption bands in the experimental spectrum. It was possible to undertake these calculations using the method of Reimers and Hush [93]. A second challenge is that the first four excited states of P^+ borrow significant intensity from the fifth excited state, by vibronic coupling. Vibronic coupling mixes transition density from a more strongly allowed transition into that of the acceptor state with sufficient spectral overlap to

acceptor excitation from B*, hence increasing the electronic coupling. In general, the Coulombic interaction between state i of molecule M and state k of molecule N, where i is vibronically mixed with state j according to the vibronic coupling parameter υ, is written as

$$V' = V_{ik}^{\mathrm{Coul}} + \upsilon V_{jk}^{\mathrm{Coul}} \tag{13}$$

where the normalization factor can be ignored when υ is small.

IV. THE PROTEIN ENVIRONMENT

A. Dielectric Screening

For a molecular aggregate, the dielectric screening must be incorporated at the level of the individual inter-site couplings. Each coupling V is multiplied by the screening factor D. Thus, for the modified Förster theory described in Section VI, dielectric screening cannot be simply incorporated in the final rate expression as can be done for a donor–acceptor system. Usually dielectric screening is assumed to have the form $D = n^{-2}$, where $n = \varepsilon_{\mathrm{R}}^{1/2}$ is the refractive index of the medium at optical frequencies [94]. This limiting expression for D is justified when the disturbances induced in the medium are of much greater wavelength than the donor–acceptor separation. It is appropriate only when V is a dipole–dipole coupling and the two chromophores are separated by a distance large compared to their sizes in a nondispersive, isotropic host medium, and local field corrections are negligible [95]. If these conditions hold, then it is likely that the system cannot be a confined molecular aggregate.

In general we suggest that the corrections introduced by the dielectric medium will be fairly small, though certain specific interactions—for example, in a protein host—may be significant. A model for medium effects on closely spaced molecules has been developed recently in our laboratory. It is suggested that for molecules that are distant from one another we can enclose each in a cavity such that the two cavities are separated by the dielectric medium. Solution of this problem leads essentially to the result $D = n^{-2}$. However, when the molecules are closely spaced relative to their sizes, we need to reconsider such a treatment. Hsu et al. [96] enclosed the pair of molecules in a cavity. They then found that the electronic coupling could be either decreased or increased, depending upon the orientation of the molecules and their positions within the cavity. In any case, because the dielectric medium is now confined to the outside of the cavity containing the dimer, the screening is smaller than for the case of well-separated molecules.

A model for large complexes in which particular pairs of chromophores may be separated by transmembrane helices has been developed by Damjanovic and

Figure 10. Dielectric model of the protein. Within this model, the protein medium (i.e., the medium with the refractive index of $n = 1.2$) is represented with a set of cylinders. The cross section of these cylinders is shown with white circles. The real location of the transmembrane part of α-helices in PSI are indicated by coiled structures. Chlorophylls are presented as Mg-chlorin rings, lacking the phytyl tail. Chlorophyll Mg atoms are shown in van der Waals representation. See color insert.

co-workers [97]. The model is best illustrated by reference to Fig. 10, which shows the distribution of transmembrance helices in Photosystem I, represented as cylinders. The heterogeneity of the protein environment is accounted for crudely by defining the site-dependent refractive index, n_{nm}, relevant for the Coulombic coupling between chlorophyll molecules n and m as follows. If the line connecting the Mg atoms of Chls n and m intercepts one of the cylinders, then $n_{\mathrm{nm}} = 1.2$; otherwise $n_{\mathrm{nm}} = 1$ in line with the arguments presented above. This model neglects possible screening by the Chl phytyl chains, and it clearly treats the protein in a highly simplified way. However, for a complex system such as PSI, it seems preferable to the standard approach of assigning a single value (usually ranging between 1.2 and 1.6) to n_{nm}.

B. Specific Interactions

Studies of the spectra and of energy transfer of site-directed mutant strains of the LH2 of *Rb. sphaeroides* have suggested that the influence of the H-bonding residues αTyr44, αTyr45 (αTyr44, αTrp45 in *Rps. acidophila*) from the adjacent α protein to the C3-acetyl group of B850 Bchl *a* contributes significantly to the

spectral shift (compared to B800 or to 777 nm in organic solvent). It was found that single (αTyr44, αTyr45 → PheTyr) and double (αTyr44, αTyr45 → PheLeu) site-specific mutations produced blue shifts of 11 and 24 nm, respectively (at 77 K) of the B850 absorption band. It has also been reported that changing the charged residue βLys23 → Gln produces an 18-nm blue shift in the B850 absorption maximum. A similar situation has been found for the B800 absorption band. Furthermore, it is the hydrogen bond from the αTyr44 to the acetyl group of βB850 which is associated with the significant distortion of this BChl *a*. The consequence of the resultant saddle conformation is a further red shift of the absorption spectrum. It is also well known that the central Mg of BChl (or Chl) should be described by a coordination number of greater than 4; that is, the Mg is typically coordinated to a Lewis base. In the case of the B850 BChls *a* of LH2, the central Mg coordinates to a His ligand. Hence it is clear that specific interactions between the BChls and certain residues play an important role in tuning the absorption spectra and, therefore, for example, in the rate of B800 to B850 energy transfer via the resultant effect on the spectral overlap integral.

In our recent *ab initio* MO studies of LH2, we found that the calculated excitation energies of B800 and the αB850 BChls (i.e., those with planar structures) are approximately the same, whereas that of the βB850 BChl were noticeably lower, presumably owing to its distorted structure. It is interesting to note that this His residue red-shifts the spectra of each monomer significantly, whereas the H-bonding ligands (αTrp and αTyr) have a lesser effect.

V. ROBUSTNESS WITH RESPECT TO DISORDER

A. Disorder in Photosynthetic Proteins

It is well known that there is significant disorder in the excitation energies from site to site and from complex to complex. This distribution of monomer energies can arise from (a) side-chain disorder in the protein, (b) deformation of the BChl macrocycle, (c) binding of ions, (d) ionizable side chains being near their p*K* values and thus existing in both neutral and ionized forms, (e) local or global distortions of the structure, and (f) the limited statistical sampling of full distribution of site energies possible in a complex of, for example, 9 or 18 monomer units.

Figure 11 shows the mean energy of 9-mer aggregates (bars) selected from a Gaussian distribution of otherwise identical monomer energies with width Δ. Clearly the distribution of 9-mer energies can be characterized by a width Σ and the relation $\Delta^2 = \Sigma^2 + \sigma^2$ holds, where σ is the width of the energy distribution within a complex. Thus for pigment problem complexes with relatively small numbers of chromophores, the static site energy distribution within a complex does not cover the entire distribution, but rather samples a subportion of the

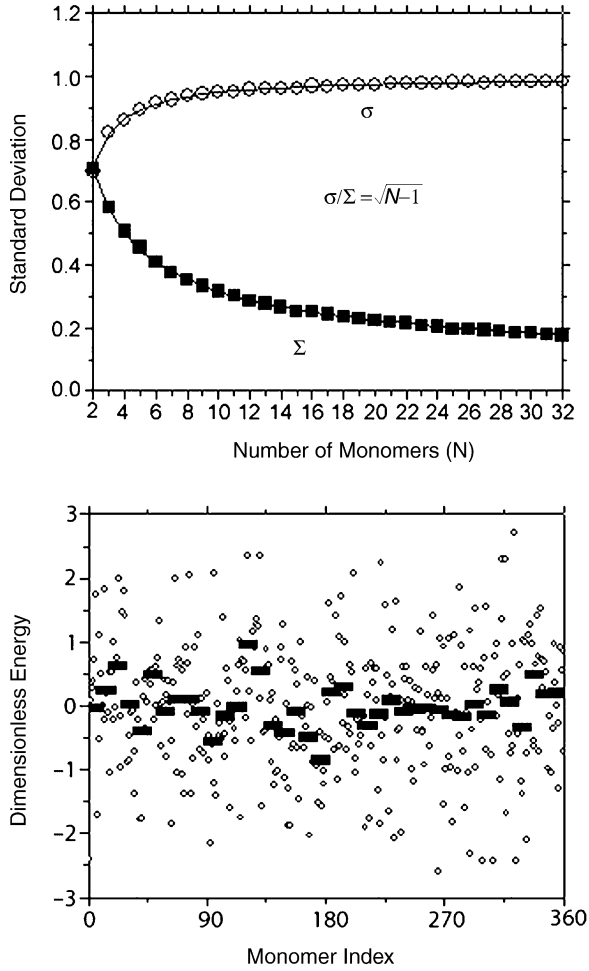

Figure 11. *Top*: Comparison of σ and the distribution width of the means, Σ, within an *N*-mer as a function of *N*. See text. *Bottom*: The mean energy of 9-mer aggregates (bars) compared to the momomer energies (circles) of distribution width σ.

total disorder. As the upper panel of Fig. 11 shows, the value of σ approaches zero for large values of the total number of pigments, N. In fact $\sigma/\Sigma = \sqrt{(N-1)}$ for $N > 1$. An absorption spectrum is only sensitive to the total value of the disorder, Δ and not the way it is partitioned between σ and Σ. Energy transfer or exciton relaxation processes within individual complexes depends only on σ, whereas Σ influences the energy transfer rate between

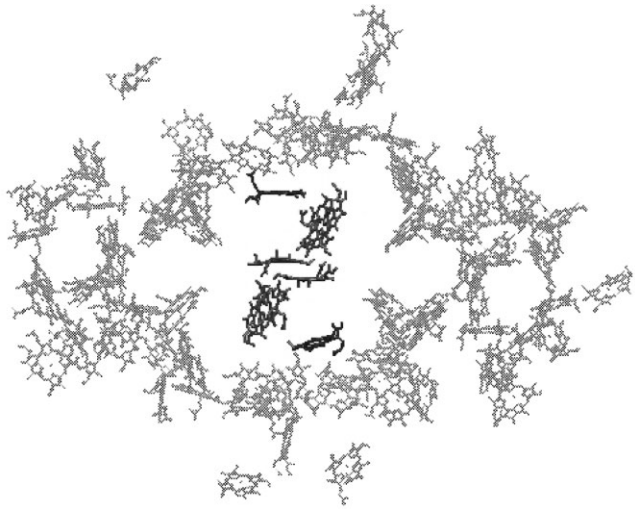

Figure 12. The organization of pigments in PS-I from the crystal structure data of Ref. 162. The reaction center is centrally located (the special pair is seen side-on). The darkest 8 Chls represent the six reaction center Chls and the two linker Chls. The linkers are the uppermost and lowermost dark Chls, respectively.

complexes. If these processes occur on different timescales, photon-echo measurements of the decay of the memory of the transition frequency can be exploited to separately determine intra- and inter-complex energy transfer dynamics as was demonstrated by Agarwal et al. [98]. The discussion above is most pertinent to complexes constructed from repeat units of one or a small number of chromophore structure ''types'' and environments such as LH2 based on an eight- or ninefold repeat of a structural element containing one B800 BChl and two B850 BChls. Photosystem I (PSI) of green plants and cyanobacteria provides a striking contrast to such a symmetric structure. In PSI, there are 96 nonequivalent Chla molecules, each in a different protein environment and with no obvious symmetry elements in the structure (Fig. 12). In addition, in contrast to LH2, the absorption spectrum of the complex is much broader than that of a dilute solution of Chla. In other words, PSI is both spatially and spectrally disordered. An additional difference between PSI and LH2 is that PSI is effectively a three-dimensional energy transfer system whereas LH2 is quasi-one-dimensional and one might expect that the disruptive effect of energy disorder on energy transfer may be different in the two cases.

This is indeed the case as the two histograms in Fig. 13 show [97]. The histograms are plots of overall excitation trapping times for 1000 different realizations of the transition energies of the Chla molecules. The transition

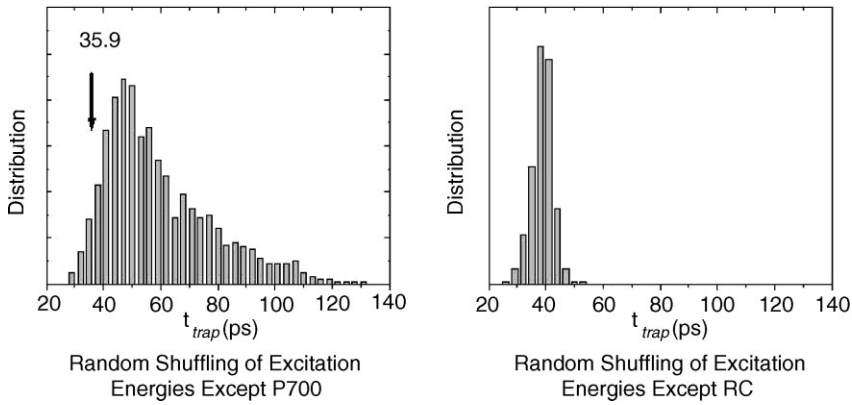

Figure 13. Distributions of trapping times (1000 samples) calculated by (*left*) a model that includes random shuffling of excitation energies in all the pigments except those of P700 and (*right*) random shuffling of excitation energies except those of the six RC pigments and the two linker Chls.

energies are taken as those obtained by Damjanovic et al. [99] via quantum chemical calculations for each individual Chla molecule. The arrow marks the calculated trapping time when the energies are assigned according to the calculation (which reproduces the absorption spectrum at both low and ambient temperatures). In the left panel, the transition energies of all Chls except P700 (the primary electron donor) are randomly shuffled. The mean value of the trapping time is 59.4 ps with a standard deviation of 18.9 ps. The distribution is asymmetric, and the energy configuration obtained by Damjanovic et al. is near the lowest bound of the distribution, suggesting that the PSI energy landscape is highly optimized for the given distribution of static energies.

A second distribution of 1000 replicas was obtained by random shuffling of the energies of the antenna Chls while the energies of the reaction center (RC) and linker Chls (see Fig. 12 and the caption) are fixed at the values calculated by Damjanovic et al. [99]. The resulting histogram of trapping times is shown in the right panel of Fig. 13. The distribution is much more symmetric and significantly narrower than the left panel. The mean and standard deviations are, respectively, 38.8 ps and 3.7 ps. From these results, we conclude that the calculated energy configuration of the reaction center and linker Chls is highly optimized and the energy configuration of the antenna Chls is highly tolerant of energy disorder because of the high connectivity of the structure. The optimality associated with the RC and the linker Chls seems to result from a quasi-energy funnel structure around the RC [97].

Of course, there must be a limit to the distribution of site energies that any given structure can tolerate at a given temperature, which relates to the ratio of

the homogeneous width of the individual transitions and the energy disorder. In fact, disorder in the antenna Chls of PSI does influence the energy transfer kinetics. A trapping time of 25.4 ps is obtained when the energies of the antenna Chls are set identical at their mean value, and the quasi-funnel structure around the RC remains as calculated. However, against the increased trapping time in the actual system (35.9 ps) the system gains total absorption cross section by extending the absorption region. The reason that the homogeneous system is so effective lies in the very small reorganization energy of Chl/protein systems, and in the next section we briefly turn to a discussion of the Stokes shift and reorganization energy of Chl molecules in protein systems.

B. Stokes Shift and Reorganization Energy

Measurement of absorption and emission spectra of the pigments in photosynthetic antenna complexes has shown that Stokes shifts are typically small [2]. Presumably this is a consequence of the solvent environment of the protein that surrounds the pigments. However, it is somewhat surprising that coupling between the pigment electronic transitions and fluctuations of the protein are so small given the key role specific pigment–protein interactions can have, such as dictating the redox potentials of pigment sin the reaction center. There are two important consequences of the small reorganization energy associated with the Stokes shift. First, the spectral overlap between like pigments is large, meaning that energy migration among the pigments in an antenna complex is very efficient. Second, excitation can be more effectively delocalized among strongly coupled pigments—for example, in the B850 ring of LH2—since excitation is localized by spectral line broadening mechanisms.

Charge transfer interactions arise in closely spaced Chl pairs. Such pairs usually exhibit strong Coulombic coupling and in addition to heterogeneity in the Coulombic coupling, the magnitudes of the electron–phonon couplings (reorganization energies) have been shown to be heterogeneous. For example, Small and co-workers [100] have shown that there are at least two types of Chla molecules in the PSI complex which are characterized by larger electron–phonon couplings than the bulk Chla because of charge transfer character in their electronic excited states. Such a variation in electron–phonon coupling strength was taken into account in the calculations of energy transfer in PSI described below [97].

Most of the information about the electron–phonon coupling comes from low-temperature spectroscopy such as hole-burning. Extrapolating these low-temperature spectral densities to room temperature can be difficult, but no determination of a room temperature spectral density for Chla has been made as far as we aware. An alternative approach is to calculate the spectral density via combined quantum mechanical/molecular mechanics calculations [99, 101], although the quantitative reliability of such an approach is not yet adequate for

detailed energy transfer calculations. At present, the best approach appears to be to use the low-temperature spectral density and make appropriate modification to fit the room temperature spectrum as described by Zucchelli et al. [102] for Chla.

C. Diagonal Disorder and Energy Transfer

To apply the Förster equation, the emission and absorption line shapes must be identical for all donors and acceptors, respectively. However, in many types of condensed-phase media (e.g., glasses, crystals, proteins, surfaces), each of the donors and acceptors lie in a different local environment, which leads to a distribution of static offsets of the excitation energies relative to the average, which persists longer than the time scale for EET. When such ''inhomogeneous'' contributions to the line broadening become significant, Förster theory cannot be used in an unmodified form [16, 63].

If there is just a single donor–acceptor pair, then we must ensemble average the nuclear spectral overlap—for example, using a Pauli master equation. One needs to think in terms of the inhomogeneous line broadening present in the donor emission spectrum and that present in the acceptor absorption spectrum leading to individually ensemble-averaged quantities. The spectral overlap is also an ensemble average quantity, and it is not related in a simple way to the overlap of the ensemble-averaged emission and absorption spectra.

In a chromophore aggregate, where there are couplings among the donor and/or acceptor chromophores, the site energy disorder affects both the electronic and the nuclear factors simultaneously. As we have described in Ref. 63, if there are m molecules that together make up the donor and n molecules that comprise the acceptor, then the EET dynamics must be determined by $m \times n$ electronic couplings. To introduce disorder properly into the EET rate calculation, each of the $m \times n$ electronic couplings $V_{\delta\alpha}$ must be associated a corresponding spectral overlap factor $J_{\delta\alpha}(\varepsilon)$. This provides us with the *dimensionless* coupling-weighted spectral overlap for each interaction, $u_{\delta\alpha}(\varepsilon) = |V_{\delta\alpha}|^2 J_{\delta\alpha}(\varepsilon)$. This quantity governs the mechanism by which EET is promoted in complex aggregates. For example, we can ascertain which electronic states most significantly mediate the EET by comparing the values of each of the $\int d\varepsilon u_{\delta\alpha}(\varepsilon)$, which are directly proportional to the rate for each pathway.

We incorporate disorder into the calculation by ensemble-averaging the set of coupling-weighted spectral overlaps for many aggregates using a Monte Carlo method [38]. In this way the effect of disorder on both electronic couplings and spectral overlap is properly accounted for by ensemble averaging $\Sigma_{\delta,\alpha} u_{\delta\alpha}(\varepsilon)$.

Energy migration among a number of chromophores with inhomogeneously broadened spectra can be modeled using a Pauli master equation approach [10, 27, 70, 71, 103–107] as long as the excitation is localized as it hops from

molecule to molecule. In such a model the probability of finding the excitation on site i in the aggregate $P_i(t)$ is determined by solving the coupled differential equations,

$$\frac{dP_i(t)}{dt} = \sum_j \left[k_{ij}P_j(t) - \left(k_{ji} + \tau_i^{-1}\right)P_i(t)\right] \tag{14}$$

where the excited state lifetime is τ_i and uphill RET rates are calculated via detailed balance, $k_{ji} = k_{ij}\exp(-\Delta E_{ij}/kT)$, with ΔE_{ij} equal to the energy difference between donor and acceptor absorption maxima. The site–site rates are calculated according to a spectral overlap involving homogeneous line shapes. A Monte Carlo sampling procedure is used to account for disorder, typically with ~2000 iterations. At each iteration the site energy offsets for each molecule in the aggregate δ_i are chosen randomly from a Gaussian distribution of standard deviation σ, $w(\delta_i) = \exp\left(-\delta_i^2/2\sigma^2\right)/\left(\sigma\sqrt{2\pi}\right)$. A Gaussian distribution is in accord with the Central Limit Theorem. It is useful to note that the FWHM of the distribution $\Delta = \sigma(8\ \ln\ 2)^{1/2}$. If the electronic coupling varies from aggregate to aggregate, because for example the molecules are oriented differently, then this can also be included.

The Pauli Master equation approach to calculating RET rates is particularly useful for simulating time-resolved anisotropy decay that results from RET within aggregates of molecules. In that case the orientation of the aggregate in the laboratory frame is also randomly selected at each Monte Carlo iteration in order to account for the rotational averaging properly.

D. Off-Diagonal (Coupling) Disorder

Disorder that affects electronic couplings is also present in chromophore aggregates. Such disorder arises from distributions of orientations and separations of the chromophores. One expects off-diagonal disorder to be most significant among closely coupled chromophores, such as those comprising B850, since orientation and distance dependencies of the coupling are most pronounced at close interchromophore separations. Once again, for EET within a chromophores aggregate, both the electronic couplings and the spectral overlaps will be by off-diagonal disorder. It is therefore rather difficult to differentiate the manifestation of diagonal from off-diagonal disorder.

Jang et al. [72] have systematically studied the effects of diagonal versus off-diagonal disorder in the B850 ring of LH2. They conclude that the diagonal disorder could be similar in magnitude to that in the B800 ring. In that case, the total disorder, observed spectroscopically to be significantly larger than that in the B800 ring, could be achieved through the addition of off-diagonal disorder.

VI. CALCULATIONS OF ENERGY TRANSFER RATES

A. Preface

Typically, light-harvesting complexes contain many chromophores in close proximity, among which energy is funneled. To relate the structures of photosynthetic antennae to a functional model requires a theoretical framework that is able to capture the essential physics. Förster theory for EET is very appealing because it is compact and simple and has few adjustable parameters. Förster theory has proven to be enormously successful for calculating EET rates between donor–acceptor pairs, but it has been observed numerous times that Förster theory cannot rationalize EET dynamics observed in chromophore aggregates. In recent work we have shown that the theory must actually be modified in order to model EET in chromophore assemblies. Photosynthetic light-harvesting proteins provided the inspiration for this work and have been a valuable testing ground to prove the quantitative utility and robustness of the theory.

B. Rate Expression for Singlet–Singlet Energy Transfer in an Aggregate

We have generalized Förster theory so that it is possible to calculate rates of energy transfer in molecular aggregates. The Generalized Förster Theory (GFT) was inspired by the ideas that (i) often weak coupling interactions promote energy transfer—because intramolecular reorganization tends to trap and localize excitation on a donor, simultaneously destroying memory effects—and (ii) in a molecular aggregate it is not necessarily clear what entities really are the energy donors and acceptors. We reasoned that there can be a mixture of weak and strong electronic couplings in a molecular aggregate. The strongly coupled molecules will exhibit collective spectroscopic properties, and the eigenstates of these coupled molecules thus collectively constitute energy donor or acceptor states. We refer to these collective states as the effective donor and acceptor states, δ and α respectively. By partitioning the Hamiltonian of the aggregate in this way, we find that the electronic couplings connecting the effective donor and acceptor states are indeed weak. Thus energy transfer from δ to α may be estimated by a Fermi Golden Rule expression, in the spirit of Förster theory. The GFT reveals that the donor emission and acceptor absorption spectra cannot be used to directly to quantify the rate of energy transfer in molecular aggregates, which has helped to explain much of the confusion in the literature regarding the explanation of observed energy transfer rates in photosynthetic proteins, as we describe in the following sections. Instead, we must turn to a ''electronic coupling-weighted spectral overlap'' between effective donors and acceptors, as we describe below. A fundamental feature of the GFT is that the organization of the molecules in the aggregate is explicitly accounted for in the

Hamiltonian. The final ingredient in the GFT is to include a correct ensemble averaging procedure to account for static disorder in the donor and acceptor transition frequencies; we implement this in the site representation.

We showed that for an aggregate consisting of m donor molecules and n acceptor molecules, we can divide the problem into interactions between effective donor and acceptor eigenstates, so that at least $m \times n$ energy transfer pathways must be considered [16, 63]. In the limit that the interactions between each pair of molecules is very weak, such that the donor and acceptor absorption spectra are unperturbed from that of the monomers, then the energy transfer rate is a sum of Förster rates. Otherwise we consider electronic couplings and spectral overlaps for each pair of eigenstates. We still think in the Förster picture, but we explicitly account for each donor emission and acceptor absorption process. For example, in B800 $\rightarrow$ B850 energy transfer, the donor is a single B800 bacteriochlorophyll, and the acceptor is the ground state of the B850 ring of 18 bacteriochlorophylls. Thus we must consider the de-excitation of B800 and excitation into each of the 18 B850 eigenstates. We note that this energy transfer involves transfer into the B850 eigenstates, so discussion of delocalization length with respect to this process is redundant. However, as described by Kühn and Sundström [108], this transfer process does involve most of the B850 ring. Dynamic relaxation processes follow the energy transfer event. An expression for the rate of energy transfer from donor states δ to acceptor states α that incorporates all these concepts given by,

$$k = \frac{2\pi}{\mathrm{h}} \left\langle \int_0^\infty \mathrm{d}\varepsilon \ \sum_{\delta,\alpha} P_\delta |V_{\delta\alpha}(\varepsilon_\mathrm{d}, \varepsilon_\mathrm{a})|^2 J_{\delta\alpha}(\varepsilon, \varepsilon_\mathrm{d}, \varepsilon_\mathrm{a}) \right\rangle_{\varepsilon_\mathrm{d},\varepsilon_\mathrm{a}} \tag{15}$$

where $V_{\delta\alpha}$ are the electronic couplings between the effective donors and acceptors, as described in Refs. 17, 63, and 64, and ε_d and ε_a represent static offsets from the mean of the donor and acceptor excitation energies as described in the previous section. Thus it is emphasized that both the couplings and the spectral overlaps depend upon disorder. It is assumed that each $V_{\delta\alpha}(\varepsilon_\mathrm{d}, \varepsilon_\mathrm{a})$ does not vary across the energy spectrum of its corresponding $J_{\delta\alpha}(\varepsilon, \varepsilon_\mathrm{d}, \varepsilon_\mathrm{a})$. P_δ is a normalized Boltzmann weighting factor for the contribution of δ to the thermalized donor state,

$$P_\delta = \exp[(\varepsilon_{\delta=1} - \varepsilon_\delta)/kT] / \sum_\delta \exp[(\varepsilon_{\delta=1} - \varepsilon_\delta)/kT].$$

The angle brackets denote that an ensemble average is taken over many aggregate units (e.g., RC complexes) so as to account for static disorder in the

monomer site energies. The spectral overlap between bands δ and α is defined in terms of donor and acceptor densities of states as in Eq. (6):

$$J_{\delta\alpha}(\varepsilon, \varepsilon_d, \varepsilon_a) = N_\alpha a_\alpha^{\text{hom}}(\varepsilon, \varepsilon_a) N_\delta f_\delta^{\text{hom}}(\varepsilon, \varepsilon_d) \tag{16}$$

Note that each $J_{\delta\alpha}(\varepsilon, \varepsilon_a)$ is associated with an electronic coupling factor $V_{\delta\alpha}(\varepsilon_d, \varepsilon_a)$ within the ensemble average. The $f_\delta^{\text{hom}}(\varepsilon, \varepsilon_a)$ and $a_\alpha^{\text{hom}}(\varepsilon, \varepsilon_d)$ specify the donor and acceptor densities of states (D.O.S.), as described in Ref. 63. The dependence upon disorder is assumed to introduce a static offset of the origin, as is usually assumed. These D.O.S. represent the emission (absorption) line shape of the donor (acceptor), calculated without disorder (hence the superscript "hom") and without dipole strength. N_δ and N_α are area normalization constants such that $1/N_\delta = \int_0^\infty d\varepsilon f_\delta^{\text{hom}}(\varepsilon)$ and $1/N_\alpha = \int_0^\infty d\varepsilon a_\alpha^{\text{hom}}(\varepsilon)$.

Our procedure requires as input a site representation of the electronic Hamiltonian that we can modify by adding disorder to the site energies. Using this "disordered" Hamiltonian, we find the set of effective donor states δ, effective acceptor states α, and the couplings between them $V_{\delta\alpha}(\varepsilon_d, \varepsilon_a)$. We can think of the $\{\delta\}$ as collectively comprising the donor emission spectrum, and we can regard the $\{\alpha\}$ as collectively comprising the acceptor absorption spectrum. For each δ and α we wish to calculate $|V_{\delta\alpha}(\varepsilon_d, \varepsilon_a)|^2 J_{\delta\alpha}(\varepsilon, \varepsilon_d, \varepsilon_a)$, the dimensionless quantity that defines the rate of $\delta \to \alpha$ EET. For this strategy to work, the $V_{\delta\alpha}$ must be classified as "weak." To determine $J_{\delta\alpha}(\varepsilon, \varepsilon_d, \varepsilon_a)$, we need electron–phonon coupling information together with intramolecular vibrational information in terms of a line-shape function or spectral density that relates to the eigenstate representation. We can input this information using explicit equations, as we do in Refs. 16, 17, and 63, but since the line-shape information is contained in experimental emission and absorption spectra (in the absence of significant inhomogeneous line broadening), experimental spectra may also be used in some cases (e.g., see Refs. 17 and 83).

C. Energy Transfer in a Complex with Heterogeneous Coulombic Coupling

Calculations of energy transfer rates and mechanisms are generally based on perturbation theory. In a dimer system with weak coupling, Forster theory can be successfully applied. However, when the Coulombic coupling is stronger than the electron–phonon coupling strength, Redfield theory [109–120] is more appropriate. In this case, the energy transfer (or exciton relaxation) is induced by the electron–phonon coupling. Yang and Fleming have shown how the Redfield and Forster theories can be combined to reasonably describe energy transfer dynamics over a wide range of parameters [121]. Based on these ideas, we describe below a strategy for calculating energy transfer dynamics in systems with a wide range of Coulombic couplings.

We begin with an overall molecular Hamiltonian $H = H^{\mathrm{el}} + H^{\mathrm{Coul}} + H^{\mathrm{el-ph}} + H^{\mathrm{ph}}$ where H^{el} and $H^{\mathrm{el-ph}}$ describe the static electronic excitations and the electron–phonon coupling respectively. H^{Coul} is the Coulombic coupling and H^{ph} is the phonon Hamiltonian.

$$H^{\mathrm{el}} = \sum_{n=1}^{N} |e_n\rangle \varepsilon_n \langle e_n|, \;\; H^{\mathrm{el}-ph} = \sum_{n=1}^{N} |e_n\rangle u_n \langle e_n| \tag{17}$$

where $|e_n\rangle$ represents the excited electronic states of the nth monomer. Within the monomer n, ε_n is its excited state energy and u_n is the electron–phonon coupling.

$$H^{\mathrm{Coul}} = \sum_{n=1}^{N} \sum_{m>n}^{N} J_{nm}(|e_n\rangle\langle e_m| + |e_m\rangle\langle e_n|) \tag{18}$$

where J_{nm} is the Coulombic coupling between $|e_n\rangle$ and $|e_m\rangle$. Our strategy is to split the Coulombic Hamiltonian into two groups of pairwise interactions: the strong Coulombic Hamiltonian, $H^{\mathrm{Coul},S}$, and the weak Coulombic Hamiltonian, $H^{\mathrm{Coul},W}$,

$$H^{\mathrm{coul}} = H^{\mathrm{coul},S} + H^{\mathrm{coul},W}$$

where if $J_{\mathrm{nm}} \geq J_{cutoff}$, we have $H_{\mathrm{nm}}^{\mathrm{Coul},S} = J_{\mathrm{nm}}$, and $H_{\mathrm{nm}}^{\mathrm{coul},W} = 0$, and if $J_{\mathrm{nm}} < J_{cutoff}$, we have $H_{\mathrm{nm}}^{\mathrm{Coul},S} = 0$ and $H_{\mathrm{nm}}^{\mathrm{Coul},W} = J_{\mathrm{nm}}$. Thus the total Hamiltonian is rewritten as

$$H = H^{\mathrm{el}} + H^{\mathrm{Coul},S} + H^{\mathrm{ph}} + H^{\mathrm{el-ph}} + H^{\mathrm{Coul},W} \tag{19}$$

Next this Hamiltonian is expressed in the basis set of exciton states obtained by numerical diagonalization of $H^{\mathrm{el}} + H^{\mathrm{Coul},S}$.

$$|\mu\rangle = \sum_{n=1}^{N} \phi_{\mu n}|n\rangle \qquad \text{for } \mu = 1, \ldots\ldots, N \tag{20}$$

where $|n\rangle = |e_n\rangle \Pi_{M=1,\, M\neq n}^{N} |g_m\rangle$ represents a state where only the nth molecule is excited and all others are in their ground ($|g\rangle$) states. $\phi_{\mu n}$ is the amplitude of the nth Chl molecule's contribution to the μth exciton state. For example, if an exciton state μ is completely localized on one molecule, say M, then $\phi_{\mu m} = \delta_{\mathrm{nm}}$. This is the case for all Chls with $H^{\mathrm{Coul},S} = 0$. If the state is equally delocalized over two Chls, k and m, $\phi_{\mu n} = (\delta_{\mathrm{nm}} + \delta_{nk})/\sqrt{2}$. In the new representation we

have diagonal $\left(H^0 = \sum_{\mu=1}^{N} |\mu\rangle H_\mu^0 \langle\mu|\right.$ and off-diagonal $\left(H' = \sum_{\mu,\mu'\mu\neq\mu'} |\mu\rangle H'_{\mu\mu'}\langle\mu'|\right.$ Hamiltonians:

$$H_\mu^0 = E_\mu + H^{\mathrm{ph}} + \langle\mu|\left(H^{\mathrm{el-ph}} + H^{\mathrm{coul},W}\right)|\mu\rangle \tag{21}$$

$$H'_{\mu\mu'} = \langle\mu|\left(H^{\mathrm{el-ph}} + H^{\mathrm{coul,W}}\right)|\mu'\rangle \tag{22}$$

In the diagonal term $\langle\mu|H^{\mathrm{el-ph}}|\mu\rangle$ and $\langle\mu|H^{\mathrm{coul,W}}|\mu\rangle$ are responsible, respectively, for the energy fluctuation and energy shift of the state μ. These diagonal parts are treated nonpertubatively. The off-diagonal term is responsible for energy transfer between exciton states. The magnitude of the off-diagonal Hamiltonian involves the strengths of the electron–phonon (μ_n) and Coulombic (J_{nm}) couplings and also the overlap of the exciton wavefunctions $\phi_{\mu n}\phi_{u'n}$. A perturbative approach to the energy transfer calculation is justified even when $\mu_n$and J_{nm} are large, provided that the overlap of the two exciton wavefunctions is small. Thus, the energy transfer rate from a state μ' to a state μ, $k_{\mu\leftarrow\mu'}$, can be calculated via the Golden Rule.

$$k_{\mu\leftarrow\mu'} = 2\,\mathrm{Re}\int_0^\infty d\tau Trq\left(e^{iH_{\mu'}^0\tau}H'_{\mu'\mu}e^{-iH_\mu^0\tau}H'_{\mu\mu'}, \rho_{\mu'}^{eq}\right) \tag{23}$$

where Tr_q denotes a trace over the nuclear degrees of freedom and $\rho_{\mu'}^{eq} = e^{-\beta H_{\mu'}^0}/Tr_q\left(e^{-\beta H_{\mu'}^0}\right)$ with β the Boltzmann factor. Yang derived an expression for $k_{\mu\leftarrow\mu'}$ in terms of standard line-broadening functions of the Chl molecules [121]. The resulting expression satisfies detailed balance. The full expression is given in Ref. 121.

When the exciton states are localized on individual Chls, the expression reduces to the well-known Förster formula. If $J_{cutoff} \to \infty$ this holds for all transfer rates. On the other hand, when $J_{cutoff} \to 0$, the expression reduces to that derived from modified Redfield theory. It can be shown analytically that the forward and backward rates satisfy the detailed balance condition

$$\frac{k_{\mu'\leftarrow\mu}}{k_{\mu\leftarrow\mu'}} = e^{-\beta\left(E_{\mu'}^0 - E_\mu^0\right)} \tag{24}$$

where $E_\mu^0 = E_\mu + H_{\mu\mu}^{\mathrm{Coul},W} - \lambda_{\mu\mu,\mu\mu}$ corresponds to the $0-0$ transition energy of the state μ. Thus once downhill rates are calculated via numerical integration, the corresponding uphill rate can be calculated from the detailed balance expression.

The precise value of the cutoff interaction energy might be considered problematical. However, as Fig. 14 shows, for a model dimer system, the modified Redfield theory and Forster theory rates are very similar over a wide range of energy gaps (degrees of delocalization); and provided that J_{cutoff}

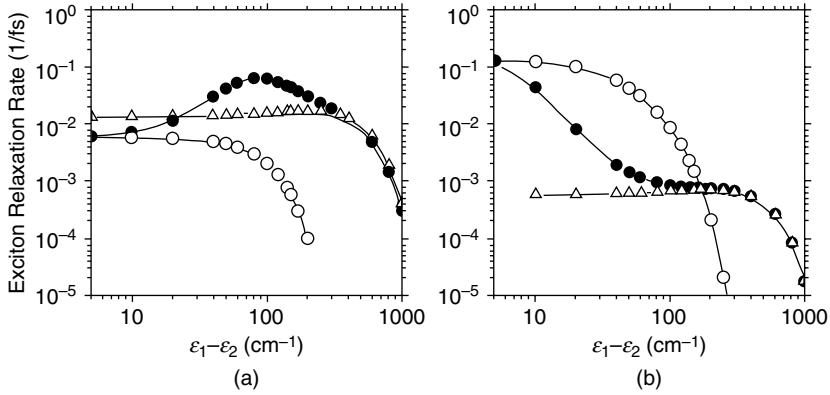

Figure 14. Downhill exciton relaxation rates as a function of energy gap between two monomers, predicted by the Förster model (open triangles), the traditional Redfield model (open circles), and the modified Redfield model (filled circles). In (*a*) the electronic coupling, $|J_{12}| = 100\,\text{cm}^{-1}$ and in (*b*) $|J_{12}| = 20\,\text{cm}^{-1}$. The reorganization energy, $\lambda = 100\,\text{cm}^{-1}$ and the spectral density is represented by a Gaussian correlation function with $\tau_g = 100\,\text{fs}$ [163].

corresponds to reasonably weak coupling, the precise value of J_{cutoff} is not critical.

This theory connects with the modified Förster theory for molecular aggregates as follows. The J_{cutoff} procedure partitions the system into the set of effective donors δ and the effective acceptors α. Whether a state is designated δ or α is determined by the excitation conditions. Energy transfer from δ to α occurs as described by Eq. (15). However, the Redfield theory can account for more complex dynamics that arise owing to competition between relaxation in the δ manifold and δ-to-α energy hopping. In other words, the multistep evolution of the excited-state population subsequent to excitation can be followed in an arbitrarily large molecular aggregate.

D. Energy Transfer to a Dimeric Acceptor: Bacterial Reaction Centers

The photosynthetic reaction center (RC) of purple bacteria is a pigment–protein complex present in the thylakoid membrane that efficiently accepts excitation energy from antenna complexes to initiate light-induced charge separation from the primary electron donor (P); this is the first step in photosynthesis. Excitation of the primary electron donor, a bacteriochlorophyll dimer, to form the lowest excited singlet state (P*) usually occurs by energy transfer from the antenna. In isolated RCs, P* can quench excitation by rapid EET from higher-energy RC pigments, either from the monomeric ''accessory'' bacteriochlorophyll-*a* molecules (B_L and B_M) or from the bacteriopheophytins (H_L and H_M). The

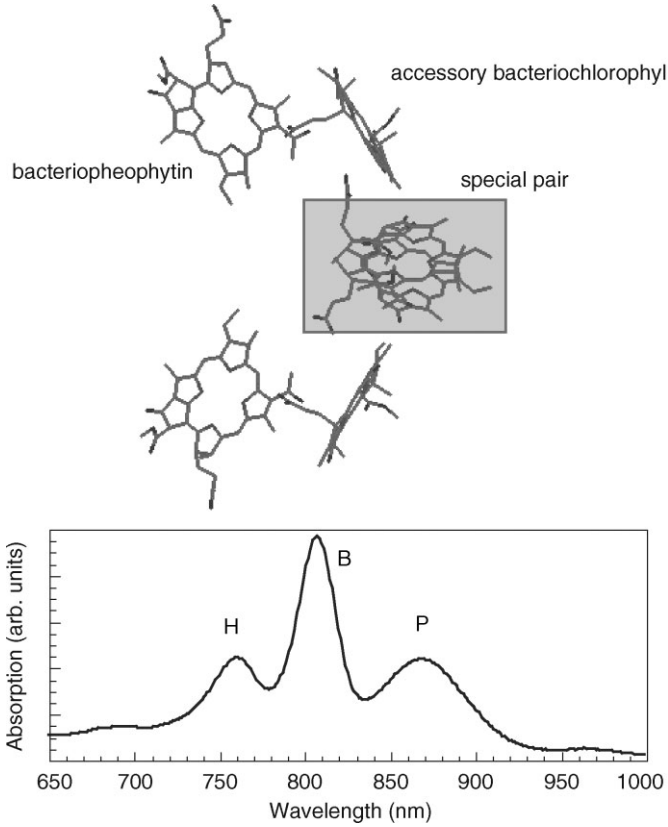

Figure 15. *Top*: Arrangement of pigments in the reaction center *Rb. Sphaeroides*. *Bottom*: Plot of the absorption spectrum of this RC, with absorption features attributed to the pigments H, B, and P indicated.

arrangement of these pigments and the absorption spectrum of the RC are shown in Fig. 15.

As early as 1972, Slooten, using absorption measurements, proposed that electronic energy transfer (EET) from H and B to P occurs in the *Rb. sphaeroides* RC [59]. In 1986 such energy transfer was shown to occur from B to P for the RC of *Rps. viridis* in less than 100 fs at 298 K. Two years later, Breton *et al*. [44] demonstrated a similar result at 10 K for the same species. Within the time resolution of these experiments, the energy transfer time was insensitive to temperature.

A consensus exists that the usual application of Förster theory is deficient by as much as an order of magnitude in accounting for the rate of EET between the

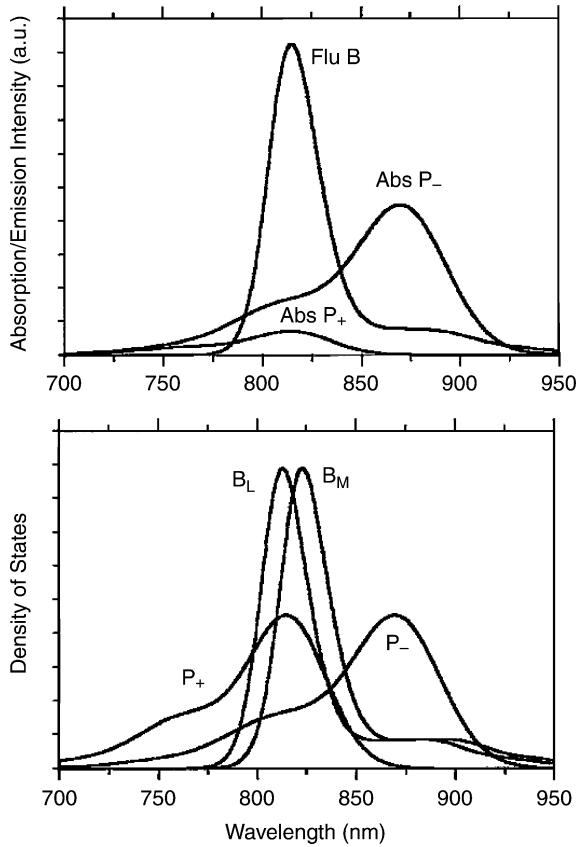

Figure 16. *Top*: The absorption spectra of the special pair acceptor states P_+ and P_- plotted over the fluorescence of the donor B. Although P_+ has superior spectral overlap with B, it has a small intensity because it is dipole-forbidden. *Bottom*: The density of states calculated for the donors and acceptors in B-to-P energy transfer. See Ref. 17.

RC cofactors. This comes about because the lower exciton state of P, P_-, carries 88% of the dipole strength and is therefore strongly coupled to B according to the dipole approximation, but has only a small overlap with the B emission, as shown in Fig. 16. The net effect is that P_- is not predicted to be an effective acceptor for B. On the other hand, the upper exciton state P_+ overlaps significantly with B emission (see Fig. 16), but since it carries only 12% of the total dipole strength, this state is predicted to be too weakly coupled to B to be an effective acceptor. The answer to the conundrum lies in the idea that the absorption spectra of the P acceptor states do not contain the

relevant information for predicting the electronic coupling between B and P_+ or P_-.

Recently the theory for EET in molecular aggregates was applied to wild-type and mutant photosynthetic reaction centers (RCs) from *Rb. sphaeroides*, as well as to the wild-type RC from *Rps. viridis*. Calculations of EET in two mutants, (M)L214H or the beta mutant and (M)H202L or the heterodimer, were also reported. Experimental information from the X-ray crystallographic structure, resonance Raman excitation profiles, and hole-burning measurements were integrated with calculated electronic couplings to model the EET dynamics within the RC complex. To check the model, which contains no adjustable parameters, optical absorption and circular dichroism spectra were calculated at various temperatures between 10 K and room temperature and compared well with the experimentally observed spectra. The rise time of the lower exciton state of P, P_-, population, subsequent to the excitation of the accessory bacteriochlorophyll, B, in *Rb. sphaeroides* (*Rps. viridis*) wild-type at 298 K was calculated to be 193 fs (239 fs), which is in satisfactory agreement with experimental results. The calculations suggest that the upper exciton state of P, P_+, plays a central role in trapping excitation from B. Our ability to predict the experimental rates was partly attributed to a proper calculation of the spectral overlap $J_{\delta\alpha}(\varepsilon)$ using the vibronic progressions.

That work provided the following answers: (1) The EET dynamics in the RC are promoted via a weak-coupling mechanism. Most importantly, we had to adapt Förster theory so that it could be applied to molecular aggregates like the RC. Our model employed only Coulombic couplings (aside from the coupling between P_M and P_L), and we conclude that short-range interactions, depending explicitly on orbital overlap between the pigments, are relatively unimportant for promoting EET. Crucially, we had to calculate correctly the *effective* donor–acceptor couplings and their associated spectral overlaps. Simple application of Förster theory blurs the details of the aggregate and leads to physically incorrect results. (2) Energy is transferred according to the following scheme: $H \rightarrow B \rightarrow P_+(\rightarrow P_-)$. (3) Our calculations suggest that P_+ is the principal acceptor state involved in energy transfer from B to P in the wild-type RC. (4) The temperature independence of EET can be understood now that we have correctly calculated the spectral overlap between B and P_+. This overlap governs the rate, and we have found it to be insensitive to temperature. The overlap between the B emission and P_-, where P_- is peaked at 865 nm at 298 K and at 890 nm at 10 K, is significantly affected by temperature, but is relatively unimportant in the overall dynamic process. (5) The large displacements of the vibrational modes of P make an important contribution to the EET by increasing the spectral overlap between B and P_+, which, in turn, increases the rate and plays a role in the temperature independence. (6) The same weak-coupling mechanism (i.e, the generalized Förster theory presented here) provides an

TABLE II
Calculated Electronic Couplings (cm^{-1}) Between the Accessory Bchls and the Exciton States of the Special Pair in the RC of *Rb. sphaeroides* (see Text and Ref. 17)

	Effective Couplings	Monomer B to P	Dipole–Dipole
B_M–P_-	−67	−55	198
B_L–P_-	69	76	−182
B_M–P_+	67	78	−6
B_L–P_+	83	72	−29

adequate description of EET in both the beta and heterodimer mutant, although in the case of the heterodimer, it is dependent on diminished electronic coupling between D_M and the rest of the RC pigments. In the beta mutant, where the weakly coupled H_M chromophore is replaced with a $BChl_a$, energy transfer is both quantitatively and mechanistically similar to the wild-type. However, in the heterodimer mutant, where the mutated pigment is part of a strongly coupled special pair, the energy transfer proceeds at a quite different rate along each branch. This leads to a biexponential rise of population of the P state.

The main advance that was made, however, was to calculate the electronic couplings $V_{\delta\alpha}$ in terms of the molecular composition of donor and/or acceptor aggregates, rather than treating the acceptors P_+ and P_- as point dipoles associated with each spectroscopic band. It can be seen in Table II that the effective electronic couplings $(V_{\delta\alpha})$ calculated for B to P_+ and B to P_- are approximately equal in magnitude. These couplings were determined from the full Hamiltonian of the RC, but compare closely with the "monomer B to P" couplings, which are effective electronic couplings calculated for the system consisting only of one B and the special pair. These latter electronic couplings may be compared directly with analogous dipole–dipole couplings calculated for B to P_+ and B to P_-, showing that the dipole approximation fails completely, thus explaining why Förster theory cannot predict the rate of B to P EET for the RC. But, why precisely does the dipole approximation fail in this case?

In Fig. 17 we compare transition densities calculated for the special pair upper exciton state P_+ (lower panel) and lower exciton state P_- (upper panel). The P_+ transition density has many alternating positive and negative phase regions that are averaged away by the dipole operator to give a small transition dipole moment. The P_- transition density has one region of negative phase and another region of positive phase, indicative of a dipole-allowed transition, that are averaged by the dipole operator to give a large transition dipole moment. Such an averaging over the topology of the transition density is carried out by light, which has a wavelength large compared to molecular dimensions and separations, and is therefore manifest in the absorption and emission spectra. However, if one imagines the B chromophore located near the right-hand side of

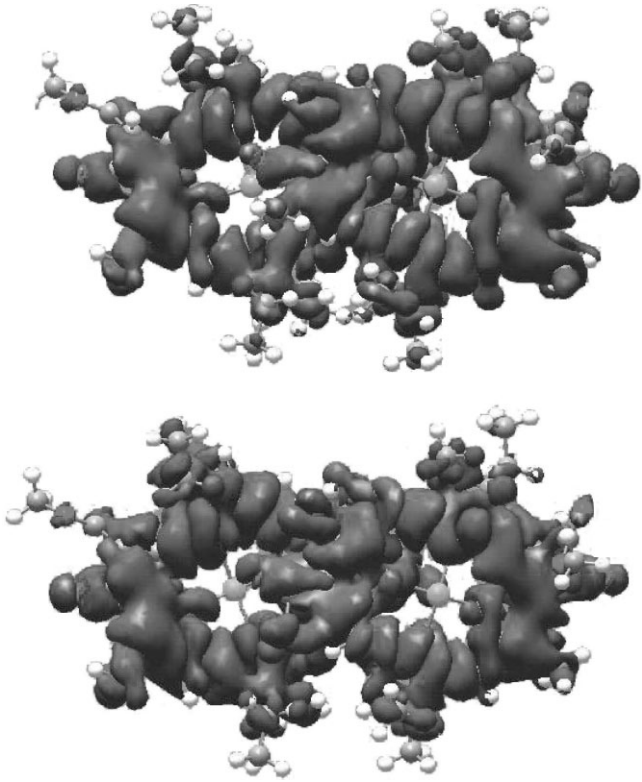

Figure 17. Transition densities calculated for the special pair. *Top*: Transition densities for P_-, *Bottom*: Transition density for P_+. See color insert.

P in Fig. 17, then it can be seen that the local P_+ and P_- transition densities that interact most significantly with the B transition are almost identical. Thus, from the viewpoint of the B donor, the electronic coupling to either P_+ or P_- should be similar, as indeed the calculations reveal.

We can summarize by stating that the averaging imposed on electronic couplings in a molecular aggregate by the dipole approximation is implemented on two levels. First, it is implemented with respect to the coupling between sites. This is the difference between panels a and b of Fig. 18, which depicts the special pair and one accessory bacteriochlorophyll of the photosynthetic RC of a purple bacterium. Panel a of Fig. 18 depicts an essentially exact calculation of the Coulombic coupling between a monomeric bacteriochlorophyll molecule k and the upper exciton state of a dimer formed by molecules m and n. This is accomplished by performing separate quantum chemical calculations of the

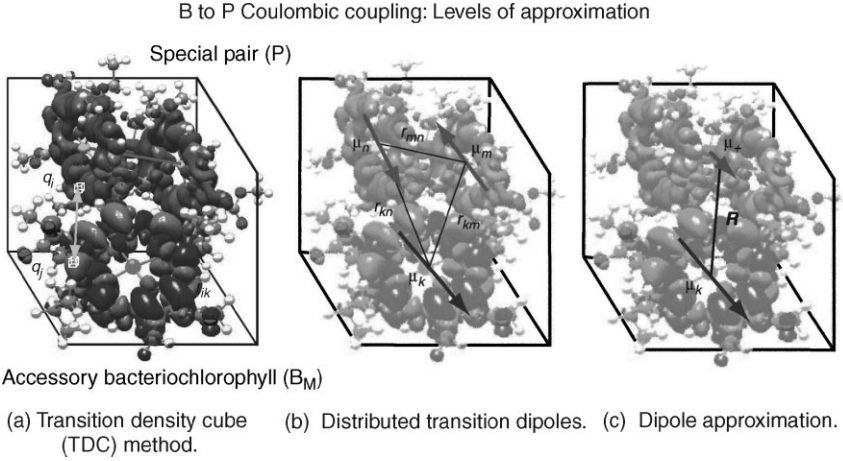

Figure 18. An illustration of the levels of approximation used in estimating the B to P_+ electronic coupling. (*a*) An essentially "exact" calculation can be made using the TDC method. (*b*) Distributed dipoles used in the GFT method (see Section VI.B) represent the minimal acceptable approximation. (*c*) The harsh dipole approximation, in which the correct physical picture of the system is completely washed away. See color insert.

ground and relevant excited states of k and the m-n dimer in order to obtain the corresponding transition densities, $P^k_{0\delta}(\mathbf{r}_1)$ and $P^{m-n}_{\alpha 0}(\mathbf{r}_2)$ respectively, which are plotted in the figure. These transition densities interact via the Coulomb potential to give the Coulombic interaction as described earlier in this review. Figure 18*b* depicts a simplification of this method, which we see as the minimal representation of this aggregate. Here the transition densities have been reduced to transition dipoles on each molecular center, according to Eq. (5). For the dimer, we need to ascertain the coefficients describing the admixture of monomer wavefunctions that comprise the dimer wavefunction, λ_m and λ_n. Then we can write $\mu_\varsigma^{\alpha 0} = \lambda_m \mu_\varsigma^{m0} + \lambda_n \mu_\varsigma^{n0}$.

Second, an averaging can be implemented with respect to the coupling within the donor or acceptor supermolecules (panel c of Fig. 18). In this case we would couple $\mu_\varsigma^{0\delta}$ and $\mu_\varsigma^{\alpha 0}$ directly. Such an averaging is invoked in analyses of RC energy transfer when, for example, either the P_- or P_+ special pair states are taken to be the energy acceptor in the Förster model, where donors and acceptors are treated as point dipoles associated with each spectroscopic band (i.e., P_+ and P_-). This approach fails to account for the true interactions within a multichromophoric assembly, as we have already described.

The Förster spectral overlap is an incredibly useful quantity for understanding EET in donor-acceptor pairs, but unfortunately it turns out to be useless for describing molecular aggregates and disordered systems. However, in the

spirit of the Förster spectral overlap, we have introduced the electronic coupling-weighted spectral overlap between effective donor and acceptor states:

$$u_{\delta\alpha}(\varepsilon) = \left\langle |V_{\delta\alpha}(\varepsilon_\delta, \varepsilon_\alpha)|^2 J_{\delta\alpha}(\varepsilon_\delta, \varepsilon_\alpha) \right\rangle_{\varepsilon_\delta, \varepsilon_\alpha}. \tag{25}$$

This quantity allows us (1) to quantify the rate of EET, according to the summation of the area of each $u_{\delta\alpha}(\varepsilon)$, as in Eq. (15), (2) identify the dominant states that mediate energy transfer in a complex system, and (3) work in terms of correctly ensemble-averaged quantities. The spectrum of the quantity $u_{\delta\alpha}(\varepsilon)$ derives from overlap of the donor emission density of states with that of the acceptor, $J_{\delta\alpha}(\varepsilon)$. This can be nonintuitive in a disordered molecular aggregate owing to the interdependence of electronic couplings and site energies, as we describe in the following section. The intensity of each spectrum is adjusted by the donor–acceptor electronic couplings. This occurs *within the ensemble average over static disorder* in the transition frequencies, ε_δ and ε_α. Now the

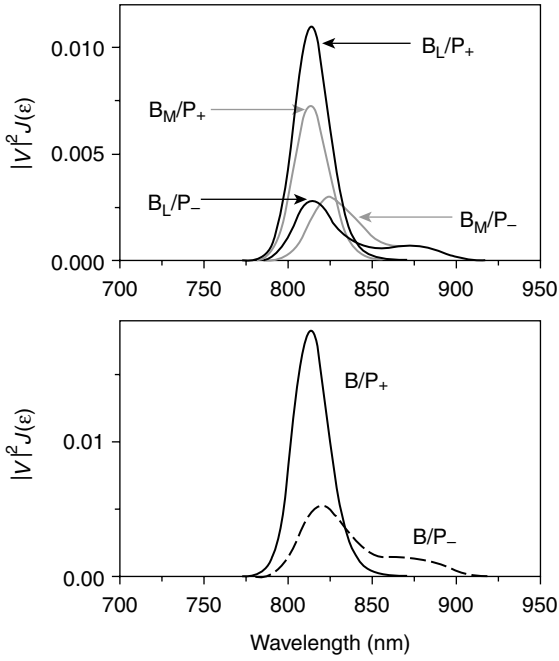

Figure 19. *Top*: Coupling-weighted spectral overlaps calculated using the GFT for all four interactions between B and P (see Ref. 17). *Bottom*: The average B to P_+/P_- picture of these coupling-weighted spectral overlaps. It is now evident that B to P_+ energy transfer dominates deactivation of initially excited B pigments.

overall area of each $u_{\delta\alpha}(\varepsilon)$ is proportional to the rate of EET via the corresponding δ–α pathway. The ensemble average coupling-weighted spectral overlaps for each of the four B to P EET pathways are plotted in Fig. 19. Inspection of the relative intensities of the $u_{\delta\alpha}(\varepsilon)$ for each pathway leads us to conclude that B to P_+ is the dominant EET channel, most likely as a consequence of better spectral overlap $J_{\delta\alpha}(\varepsilon)$.

E. Energy Transfer in LH2

1. B800 to B850 Energy Transfer

In the introduction to this review we have described in detail the structure and function of the peripheral light-harvesting antenna LH2 of purple bacteria. Light absorbed by the B800 ring is transferred rapidly to the B850 ring on a time scale of 800 fs in *Rps. acidophila* and 650 fs in *Rb. sphaeroides* at room temperature, increasing to just 1.2 ps at 77 K for both *Rps. acidophila* and *Rb. sphaeroides*. Förster theory, however, provides an unsatisfactory estimate of this time scale and, in particular, fails to elucidate the reasons for the remarkable insensitivity to temperature.

The donor molecule of the B800 ring is approximately monomer-like and is located ∼18 Å away from the acceptor. The acceptor consists of the 18 bacteriochlorophylls of the B850 ring, part of which is shown in Fig. 20. The

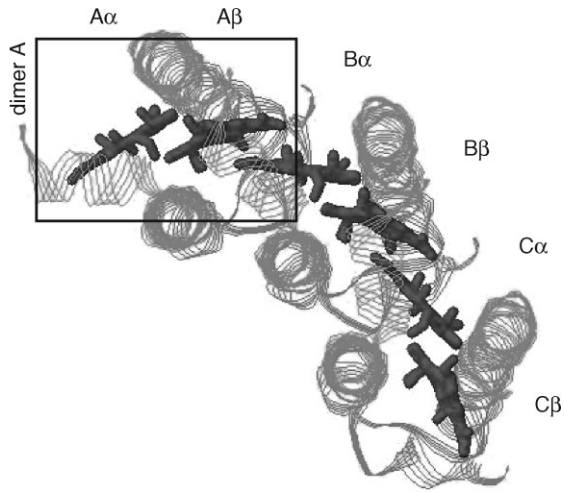

Figure 20. A depiction of part of the B850 ring from LH2 showing the α-helices as ribbons, labeled as α and β according to their position on the inside and the outside of the ring, respectively. The pigments are labeled A, B, C according to the α,β-subunit they belong to, and they are labeled individually as α or β according to whether they are coordinated to the α-helix labeled α and β. The close interaction (3–4 Å) between these Bchl chromophores is evident.

Bchl molecules that comprise the B850 ring are relatively strongly coupled to each other ($\sim 300\,\mathrm{cm}^{-1}$), which has a significant impact on the nature and operation of the acceptor states. This also means that there are not just one or two acceptor states: There are 18 acceptor states that must be individually considered. Moreover, each LH2 complex is slightly different spectroscopically, owing to significant inhomogeneity in the site energies of each Bchl. The effect of this static disorder on the absorption is shown by the absorption spectra calculated for individual LH2 complexes (Fig. 21). These spectra are similar to the striking experimental observations reported by van Oijen et al. [16]. Any model for predicting the EET dynamics in this complex system must capture these essential features.

In order to model realistically the effective acceptor states of the B850 ring, it was first necessary to calculate the electronic couplings on the basis of the crystal structure data. Owing to the close approach of the Bchls in B850 (cf. Figs. 6 and 20), we decided to ascertain the significance of contributions to the electronic coupling that depend on orbital overlap, V^{short}. V^{short} mostly derives from interactions indicative of mixing of donor–acceptor wavefunctions

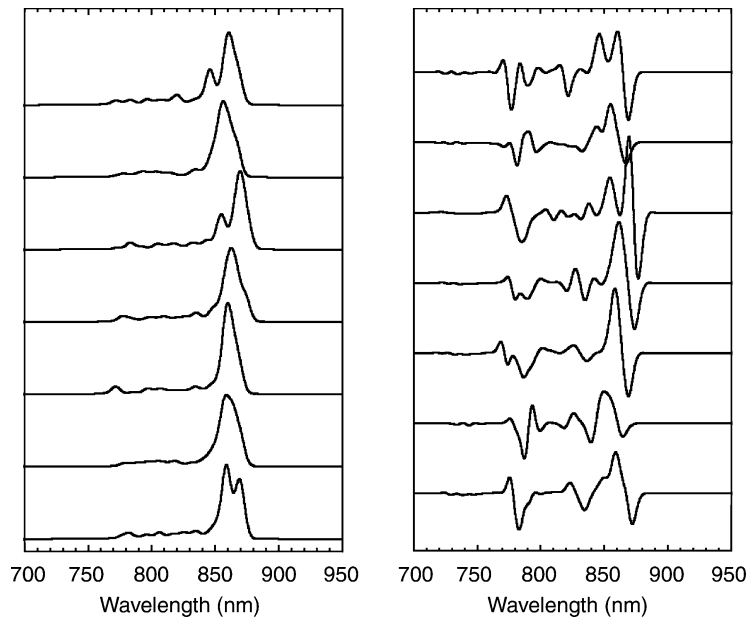

Figure 21. *Left*: Absorption spectra calculated for a random selection of single LH2 complexes (*Rps. acidophila*, 77K). *Right*: The corresponding calculated circular dichroism spectra. Only diagonal disorder is included in the site energies of the monomers, but note the dramatic effects it has on state energies and intensities.

owing to their interpenetration (exchange effects related to the Coulombic interactions make a very minor contribution for molecules). There has been considerable speculation regarding the role of V^{short} in photosynthetic light harvesting since if this coupling becomes significant relative to V^{Coul} at close separations, then the EET rate could increase over that estimated from the Förster rate by a factor $\left|V^{\text{Coul}} + V^{\text{short}}\right|^2 / \left|V^{\text{Coul}}\right|^2$. However, evaluation of the significance of the V^{short} component of the coupling by quantum chemical calculation poses a difficult problem.

We attempted to quantify the total V^{short} for the closely interacting BChl pigments in LH2 of *Rps. acidophila* using CI-singles calculations (6-31G* level) of the excited states of Bchl dimers within the B850 ring, as well as individual Bchl molecules. The dimer calculations provided an estimate of the total electronic coupling $\left(V^{\text{short}} + V^{\text{Coul}}\right)$, but where V^{Coul} was overestimated, just as for the TDC calculations based on CI-singles TDs. We could use TDC calculations, then, to determine the (overestimated) V^{Coul} and hence retrieve V^{short} (which is not similarly overestimated). The usual scaling procedure provided a reasonable estimate of V^{Coul}. We summarize our results in Table III, where we collect the scaled V^{Coul}, calculated by the TDC method, V^{short} derived from the *ab initio* supermolecule calculations once V^{Coul} had been determined, and the total electronic coupling, equal to $V^{\text{short}} + V^{\text{Coul}}$ (where this is the scaled Coulombic interaction).

Combining the calculated electronic couplings with various experimental data, we have simulated the energy transfer dynamics in the wild-type *Rps. acidophila* B800–B850 complex, as well as in four reconstituted complexes in which the B800 band lies at 765, 753, 694, and 670 nm (which we refer to as B765, B753, etc.). There are no adjustable parameters in these calculations, since the mean Bchl site energies in the B800 and B850 rings are set in order to simulate the absorption and circular dichroism spectra. The mutant and

TABLE III

Nearest-Neighbor Electronic Couplings V (cm^{-1}) Calculated Between the Bchl Q_y Transitions in the B850 Ring of the LH2[a] of *Rps. acidophila* Using the CI-singles/6-31G* Method (see Text and Ref. 74), Along with Next-to-Nearest Neighbor Couplings Calculated Using the CI-Singles/3-21G*/TDC Method [73]

	Separation[b] (Å)	Total Coupling	V^{Coul} Part	V^{short} Part	$V^{\text{dipole–dipole}}$
$\alpha B850_A$–$\beta B850_A$	9	320	265	55	415
$\beta B850_A$–$\alpha B850_B$	9.5	255	195	60	330
$\alpha B850_A$–$\alpha B850_B$	18	−46	−46	0	−48
$\beta B850_A$–$\beta B850_B$	19	−37	−37	0	−37

[a]See Fig. 20 for the labeling convention.
[b]Center-to-center.

TABLE IV
Calculated B800–B850 Energy Transfer Times (ps) in LH2 of *Rps. acidophila* and Reconstituted Complexes (See Text and Refs. 16 and 22)

	GFT[a] (77 K)	GFT[a] (300 K)	Experiment[b]	FT[c] (300 K)
B800–B850	0.96	0.91	0.9	6
B765–B850	0.76	0.75	1.4	9
B753–B850	1.90	1.34	1.8	11
B694–B850	17.3	13.8	4.4	18
B670–B850	49.6	43.7	8.3	37

[a]Generalized Förster Theory for molecular aggregates (see Section VI.A and Ref. 63).
[b]Results reported by Herek et al. [122] (300 K).
[c]Förster Theory predictions [122].

temperature dependence of the B800–B850 EET rates provides a convincing test of the theory for energy transfer in molecular aggregates, Eq. (15).

In Table IV we summarize the results of these calculations for both 77 K and 300 K. Note that here it is assumed that each of the substituted chlorophylls has the same transition moment magnitude and orientation, and therefore coupling to the B850 BChls, as the wild-type B800s. We see from the results collected in Table IV that (i) the calculated energy transfer times for B800–B850 and B753–B850 correspond closely to the experimental values reported by Herek et al. [122]; (ii) the calculated B800-B694 and B800-B670 energy transfer times are much slower than revealed by experiment, suggesting that the carotenoid S_1 state may be mediating the energy transfer for these donors; (iii) While the ''B800''-type donor has appreciable overlap with the B850 density of states, which spans 720–870 nm, the 'B800'–B850 energy transfer time is rapid and is sensitive (i.e., can be tuned by a factor of two in magnitude) to the exact location of the donor emission spectrum; (iv) The EET rate is insensitive to temperature, which is a well-known characteristic of the wild type LH2 complex.

In Fig. 22 the spectral overlaps calculated for seven individual LH2 complexes (*Rps. acidophila*) are shown and compared to the corresponding coupling-weighted spectral overlaps, calculated according to the GFT. First we note that the spectral overlaps do not correspond to the Förster spectral overlaps, since we have correctly calculated the overlap between the donor emission and the absorption density of states (not absorption spectrum) of each acceptor eigenstate according to Eq. (16), rather than as the overlap between the donor emission and total B850 absorption spectrum. Second, it is evident that a proper ensemble average over the individual complexes is crucial because of the significant static disorder, as seen in the single complex absorption spectra shown in Fig. 21. However, comparison of the calculated spectral overlaps with

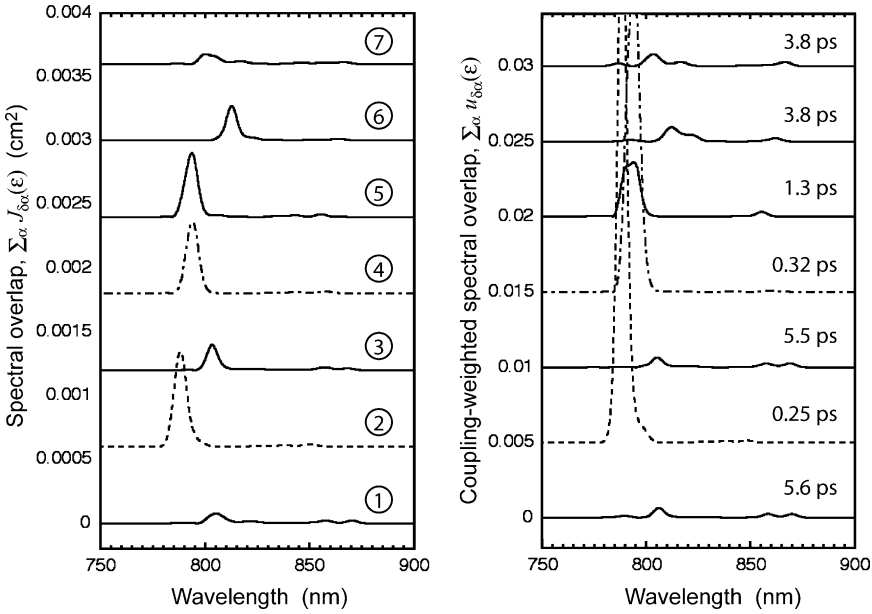

Figure 22. *Left*: Spectral overlaps calculated using the GFT model for B800–B850 energy transfer within each of the single LH2 complexes shown in Fig. 21. The dashed and dashed–dot lines for spectra 2 and 4, respectively, are simply meant to guide the eye in the right-hand panel of the figure. *Right*: Coupling-weighted spectral overlaps and energy transfer times calculated for these systems. See text.

the calculated coupling-weighted spectral overlaps immediately reveals significant differences. For example, from the spectral overlap calculations, the B800–B850 EET times for complex 4 and 5 are expected to be similar. However, a calculation according to the GFT reveals via the coupling-weighted spectral overlaps that the EET times in these two complexes actually differ by a factor of 4! Such observations emphasize the importance of keeping the electronic coupling and corresponding spectral overlap factor associated.

LH2 typifies a complex donor–acceptor system for which EET rates cannot be understood according to Förster theory. To elucidate B800–B50 EET rates, it was crucial to understand the nested averages in a microscopic picture of the dynamics that are important even at the level of single complexes. Thus, the summations over effective donor and acceptor states, and the ensemble average over disorder must be carefully treated. These subtleties are all contained in Eq. (15), the GFT, and cannot be ignored for the sake of an expedient solution. The key quantity for characterizing EET in molecular aggregates is the coupling-weighted spectral overlap, $u_{\delta\alpha}(\varepsilon)$, Eq. (25).

2. *Exciton Dynamics in B850*

In the case of the B850 molecules of LH2 or the B875 molecules of LH1, the situation is more complex. Now the excitonic interactions are at least similar to the site energy disorder, k_BT, and the electron–phonon coupling and the electronic (and perhaps vibrational) state are not localized on individual molecules. This delocalization leads to the phenomenon of exchange narrowing [123] whereby the distribution of site energies is apparently narrowed by the averaging effect of the delocalized states. Thus the intracomplex disorder, σ, and, therefore, the total disorder, becomes dependent on the electronic coupling. The intercomplex disorder Σ, however, remains independent of the coupling.

In such a system the initially prepared state can evolve very rapidly via electron–phonon coupling. This rapid relaxation among exciton levels gives rise to a kind of lifetime broadening, which competes against the exchange narrowing. The two effects cannot be separated by analysis of the linear absorption spectrum, but can be resolved by analysis of photon-echo signals [124]. Thus in order to properly characterize a system such as the B850 ring of LH2 or the B875 ring of LH1, it is necessary to be able to have a formalism with which one is able calculate both linear and nonlinear optical signals from the same approach.

Energy disorder (both diagonal and off-diagonal) plays a major role in determining the electronic structure and consequent dynamics of such a system. As before, averaging over the ensemble must be done after the microscopic dynamics are calculated. Figure 23 shows the exciton levels and associated

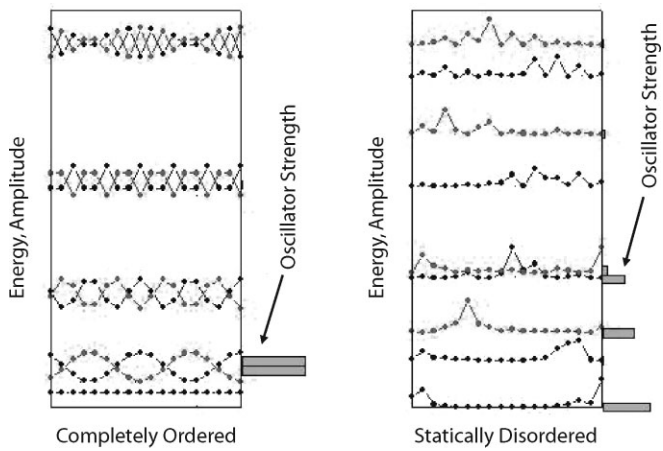

Figure 23. Exciton wavefunctions calculated for the B850 band of LH2. *Left*: For a completely ordered model with $J_{\text{intra}} = J_{\text{inter}} = 320\,\text{cm}^{-1}$. *Right*: For a statically disordered model, with $J_{\text{intra}} = 320\,\text{cm}^{-1}$, $J_{\text{inter}} = 255\,\text{cm}^{-1}$, $\sigma(\text{disorder}) = 150\,\text{cm}^{-1}$ and an energy offset between α and β Bchls (see Fig. 20) of $530\,\text{cm}^{-1}$. See Ref. 40.

wavefunctions for the B850 either as completely ordered or for a particular complex selected from a distribution with $\sigma = 150\,\mathrm{cm}^{-1}$. In the perfectly ordered case, the lowest state is optically dark and all the oscillator strength is concentrated in the next two (degenerate) levels. The wavefunctions are completely delocalized for all levels. In the disordered case, the oscillator strength is distributed over multiple levels; in particular, the lowest state is no longer dark, and the wavefunction is ''broken up'' such that it has amplitude on typically 2–4 molecules. Figure 23 is useful for visualizing the system but does not allow calculation of the dynamics or nonlinear optical response. For this, we turn to a formalism based on the density matrix and calculate the dynamics using Redfield theory [124]. The formal approach has been described in detail in Refs. 124 and 121. Here we give a brief overview of the approach beginning with theory for the linear absorption and third-order response of a simple model system for molecular aggregates which consist of monomers with two electronic states. The standard description of the electronic states of molecular aggregates is based on the Frenkel-exciton Hamiltonian.

$$H = H^{el} + H^{el-ph} + E^{ph} \tag{26}$$

$$H^{el} = \sum_{n=1}^{N} |n\rangle \varepsilon_n \langle n| + \sum_{\substack{m,n \\ m \neq n}}^{N} J_{mn} |m\rangle \langle n| \tag{27}$$

$$H^{el-ph} = \sum_{n=1}^{N} |n\rangle u_n \langle n| \tag{28}$$

where $|n\rangle$ is the electronic excited state of the monomer n and ε_n is the static energy of the electronic excited state of the nth monomer. u_n describes the fluctuation of the transition energy due to the electron–phonon coupling. E^{ph} is the Hamiltonian of the phonon bath. The interaction between monomers n and m is given by J_{mn}, which is assumed to be homogeneous. We also assume that each monomer is coupled to its own bath and that the baths belonging to different monomers are uncorrelated.

For the one-exciton state, the eigenstates and eigenenergies of the Frenkel excitons are obtained by numerical diagonalization of the electronic part of the exciton Hamiltonian [Eq. (27)]. The exciton wavefunctions and exciton energies for the two exciton band can be constructed from those of the one exciton band by use of Bethe's Ansatz [125]. The electron–phonon coupling Hamiltonian H^{el-ph} is responsible for pure dephasing of the exciton states (diagonal in exciton basis) and population transfer between the exciton states (off-diagonal in exciton basis).

The linear and third-order response functions of the molecular aggregates are described by a density matrix formalism in the exciton basis. The evolution of

the density matrix is given by

$$\frac{d}{dt}\rho(t) = -i(L_0 + L')\rho(t) \tag{29}$$

where L_0 is a diagonal Liouville operator governing the exciton dynamics in the absence of any exciton transfer process. The off-diagonal term, L', is responsible for the population transfer process between the exciton states. The usual method to obtain the time evolution of the exciton state is to reduce the full density matrix [Eq. (29)] to the excitonic space by taking an average over the bath. In this case, we lose detailed information of the dynamics of the bath. However, the photon-echo peak shift method [124] is sensitive to the non-Markovian behavior of the bath, and thus we need to keep the dynamics of the bath to accurately describe the experimental data. As a first approximation, the operator of the second term of the right-hand side of Eq. (29) is replaced with a rate equation.

$$\frac{d}{dt}\rho(t) \approx -iL_0\rho(t) - K\rho(t) \tag{30}$$

where K is the Redfield tensor which is based on a second-order approximation with respect to the off-diagonal Hamiltonian in the exciton representation [124]. Equation (30) is a kind of mean-field description of the population transfer since the phonon-dependent operator has been replaced by a phonon-averaged rate equation. We note, however, that the fast phonon dynamics is correctly described by the first term of Eq. (30) in contrast with the usual reduced density matrix approach. As usual, we introduce the so-called secular approximation in which the nonsecular elements of the Redfield tensor are assumed to be zero:

$$K_{\alpha\beta,\alpha'\beta'} = 0 \qquad \text{when} \qquad \left|\omega_{\alpha\beta} - \omega_{\alpha'\beta'}\right| \neq 0 \tag{31}$$

where $\omega_{\alpha\beta}$ is the energy difference between the states α and β. The contributions of the nonsecular terms are averaged out on a time scale of $\left|\omega_{\alpha\beta} - \omega_{\alpha'\beta'}\right|^{-1}$. By this approximation, contributions for the population and coherence elements are not likely to be coupled to each other in the presence of static disorder. The Redfield tensors then consist of three terms: (a) population transfer from α to γ ($\alpha \neq \gamma$), $K_{\alpha\alpha,\gamma\gamma}$, (b) population decay from α, $K_{\alpha\alpha,\alpha\alpha}$, and (c) decay of the coherence (dephasing) due to population transfer, $K_{\alpha\alpha',\alpha\alpha'}$.

For the linear absorption spectrum, the system evolves in a coherence between the ground and one-exciton states after the interaction with the first pulse. Exciton relaxation occurs during the coherence period and influences the

broadening of the absorption spectrum. The linear absorption spectrum of an aggregate in the presence of population transfer is given by

$$I(\omega) = \mathrm{Re}\int_0^\infty dt \exp(i\omega t) \sum_{k=1}^{N} \left|d_{gk}\right|^2 \exp\left[-iE_k t - g_{kk}(t) - K_{kk,kk}t\right] \qquad (32)$$

where $K_{kk,kk}$ is the population decay rate from the kth level of the one exciton state and E_k is the static energy of the kth exciton state and $g_{kk}(t)$ is the exchange narrowed line-shape function which is given by

$$g_{kk}(t) = C_k g(t) \qquad (33)$$

For completely localized states, we have $C_k = 1$. Therefore the line broadening function for the aggregate is the same as that for monomer. In the absence of static disorder, we have $C_k \sim \frac{1}{N}$. In other words, the width of absorption spectrum of the aggregate becomes significantly narrower. The narrowing results from the fact that delocalized exciton states average over the disorder in the transition frequency of the individual molecules. Due to the presence of the disorder in the system, the degree of the delocalization of the exciton in the aggregates is smaller than the actual size of the aggregates.

The procedure for calculating both the linear absorption spectrum and the third-order nonlinear signals is shown schematically in Fig. 24. After diagonalizing the Hamiltonian, we construct the exciton wavefunctions and energies and calculate the transition dipole moments. Then we calculate the exciton population transfer rates from the expression for the Redfield tensor with the spectral density of the phonon. Inserting the solution of Eq. (30) into the linear and third-order response functions and taking into account the finite laser pulse duration, we calculate the third-order nonlinear signals. These procedures are repeated over different sets of static energies of the monomer until our calculated result converges.

The width of the absorption spectrum for the aggregate is significantly narrower than that for monomer as a result of the exchange narrowing. As the value of the static disorder decreases, the exciton becomes more delocalized in the aggregates and the width of the absorption spectrum decreases when we only consider the exciton structure and the exchange narrowing mechanism. Now exciton population transfer contributes to the width of the absorption spectrum via lifetime broadening, and the width of the absorption spectrum no longer depends on the degree of the delocalization. The fast nuclear fluctuations of the monomers appear as exciton energy fluctuation and population transfer in the exciton basis. The energy fluctuations are subject to the exchange narrowing, and the population relaxation produces lifetime broadening. Because

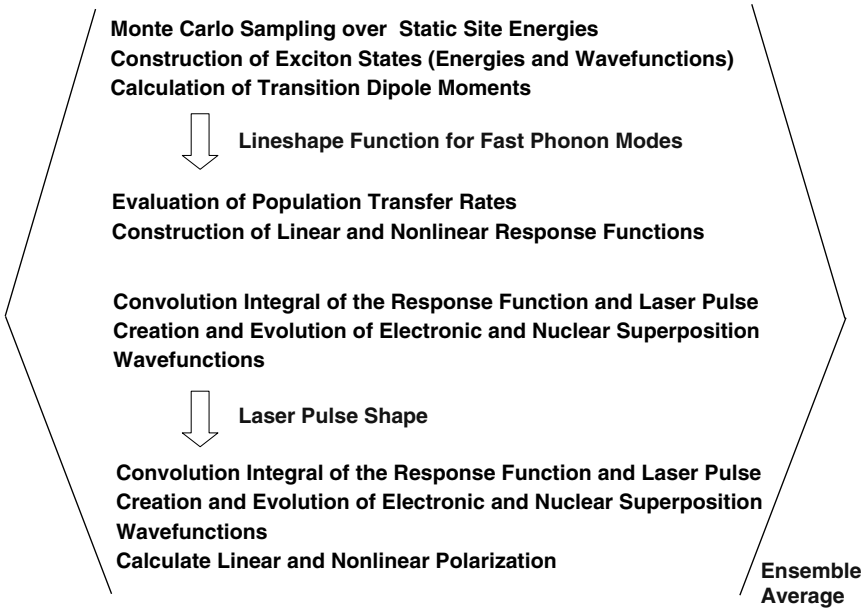

Figure 24. Schematic diagram of the procedure used to calculate the linear absorption and third-order nonlinear signals in molecular exciton systems. See Ref. 124.

of this, in contrast with static disorder (which is completely exchange-narrowed), the dynamical disorder is not completely subject to the exchange narrowing. Knoester and co-workers [126, 127] investigated the effect of the dynamic disorder in the optical line shapes for circular aggregates and arrived at a similar conclusion. For small aggregates, they found that the exchange narrowing factor is equal the number of molecules in the aggregate, while for large aggregates it saturates. The number of molecules at which it saturates depends on the amplitude of the fast fluctuation and the intermolecular coupling.

Figure 25 summarizes the processes included in the calculation in a pictorial fashion. The procedure outlined in Figs. 24 and 25 is combined with the calculated electronic couplings for B850 (Sections III.C and VI.E), a line-shape function obtained by fitting photon-echo peak shift data and static disorder from hole-burning and other experimental methods; the absorption spectrum and photon-echo peak shift decay are calculated for B850, without adjustable parameters [40] (Fig. 26). The agreement with both experimental measures is rather good, including the slow decay of the echo peak shift evident from 200 fs to 1 ps. What do the timescales evident in the peak shift decay of

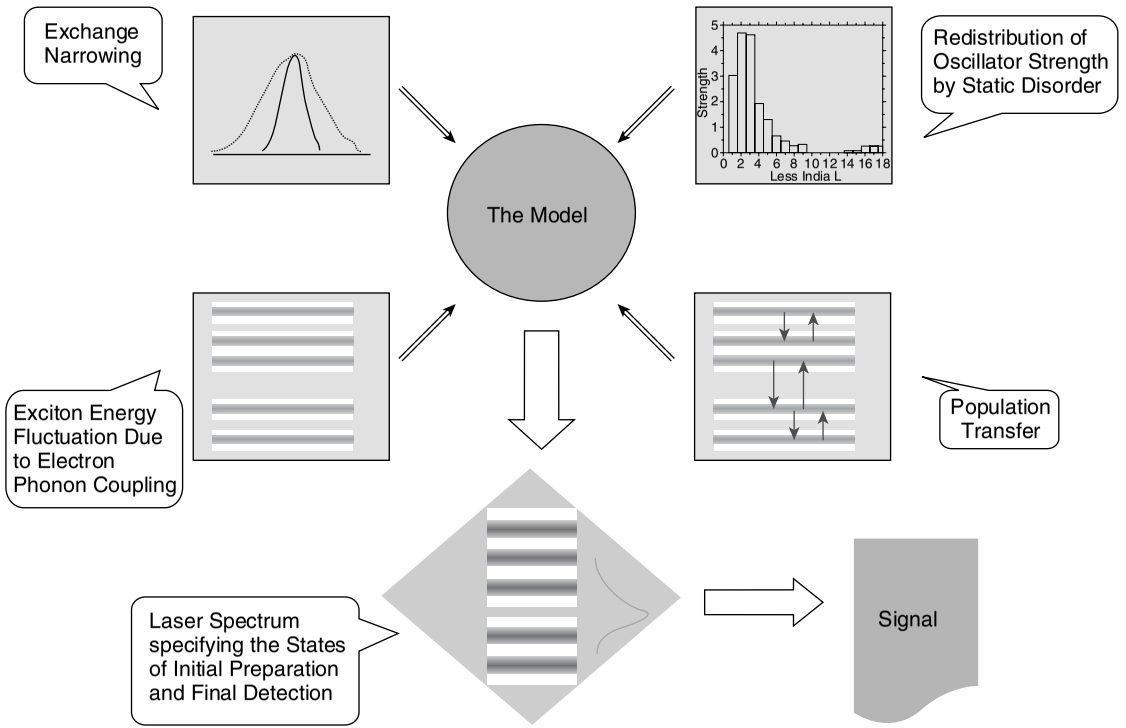

Figure 25. Pictorial representation of the calculation of exciton population and relaxation induced by pulsed laser excitation and the resulting linear and nonlinear optical signals. See text for details.

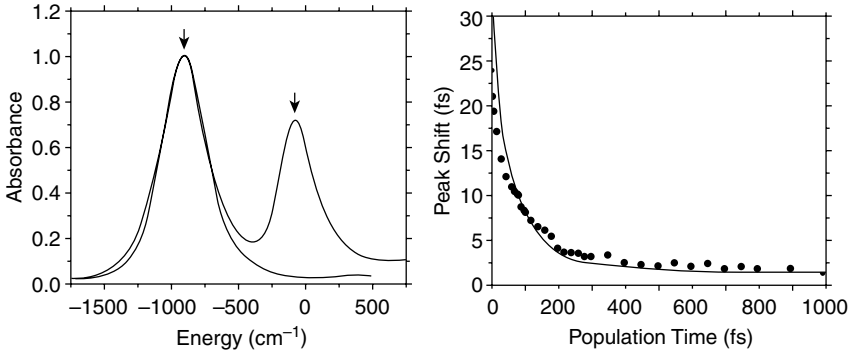

Figure 26. Comparison for the absorption spectrum and three-pulse-echo peak shift determined from experiment for the B850 band of LH2 with that calculated using the model described in the text. Parameters are the same as in Fig. 23 (*right panel*), plus a spectral density (see Ref. 40).

Fig. 26 represent? To investigate this, we consider the following ansatz: The peak shift decay ($\tau^*(T)$ versus T) can be approximated as a product of a term describing the exchange narrowing effect and a term describing population relaxation:

$$\delta\tau^*(T) \approx \frac{\tau^* exchange(T)}{\tau^* exchange(0)} \cdot \delta\xi(T) \tag{34}$$

where

$$\delta A(T) \equiv \frac{A(T) - A(\infty)}{A(0) - A(0)}$$

is a normalized peak shift on population term and

$$\xi(T) \equiv \frac{P_D(T)}{P_D(T) + P_A(T)} \tag{35}$$

where $\tau^*_{exchange}(T)$ is the echo peak shift of the exchange narrowed system when exciton relaxation is turned off, $P_D(T)$ is the weighted (by the oscillator strength and the laser spectrum) sum of population remaining on the initially prepared states, and $P_A(T)$ is the (similarly) weighted sum of the population on states transferred to that are within the laser bandwidth.

The points in Fig. 27 are calculated exactly from the full theory for two different values of the diagonal disorder. The solid lines are calculated according to the ansatz of Eq. (34). For a large value of the disorder, the

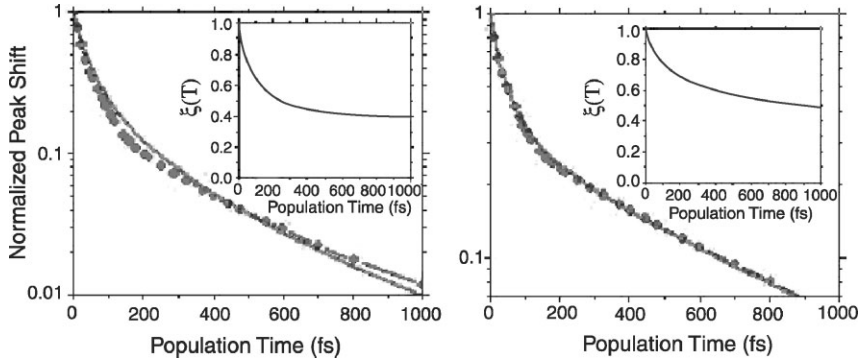

Figure 27. Illustration of the ansatz described by Eq. (34). The points represent the exact calculated photon-echo peak shift, while the solid line is calculated via Eq. (34). The insert shows the population term [Eq. (35)]. The Left panel is for a disorder (σ) of 160 cm^{-1}, and the right panel is for $\sigma = 320\,cm^{-1}$. Other parameters are as in Figs 23 and 26.

agreement between the exact result and the factored form is quantitative. For the small disorder, the two results deviate slightly, because the disorder is not large enough to entirely decorrelate the energy levels, but still the agreement is very good. The insets show the population relaxation contribution showing that both fact and slow exciton relaxation can be captured by the photon-echo peak shift method.

Finally, it is possible to make a pictorial representation of the exciton dynamics in B850 of LH2. Figure 28 shows the density matrix at 0 fs, 50 fs, and 100 fs in both the exciton basis (upper) and the site basis (lower). In interpreting Fig. 28, it is important to recall that two levels of ensemble averaging are involved in generating the microscopic observable. First, the density matrix approach averages over the fluctuations induced by the phonon modes, and, second, after the phonon-averaged molecular response is calculated, an average over the static disorder is required. The plots in Fig. 28 contain only the first average. Turning to the plots themselves, note that the initial excitation is highly delocalized with two nodes evident in the site basis at the position of monomers whose transition dipoles lie perpendicular to the excitation polarization. Within 50 fs, the excitation becomes localized on groups of 2–4 molecules (site basis), and the coherence evident in the off-diagonal $(k \neq k')$ amplitudes in the exciton basis has almost disappeared. By 100 fs, the exciton representation is almost fully diagonal and the exciton populations (diagonal terms) have redistributed. The clear localization to 2–4 molecules in the site representation suggests that a reasonable physical image of the dynamics can be visualized via Fig. 23. Noting that the Redfield equations for the population relaxation contain the overlap of the wavefunctions of the initial and final states, the picture emerges of excitation

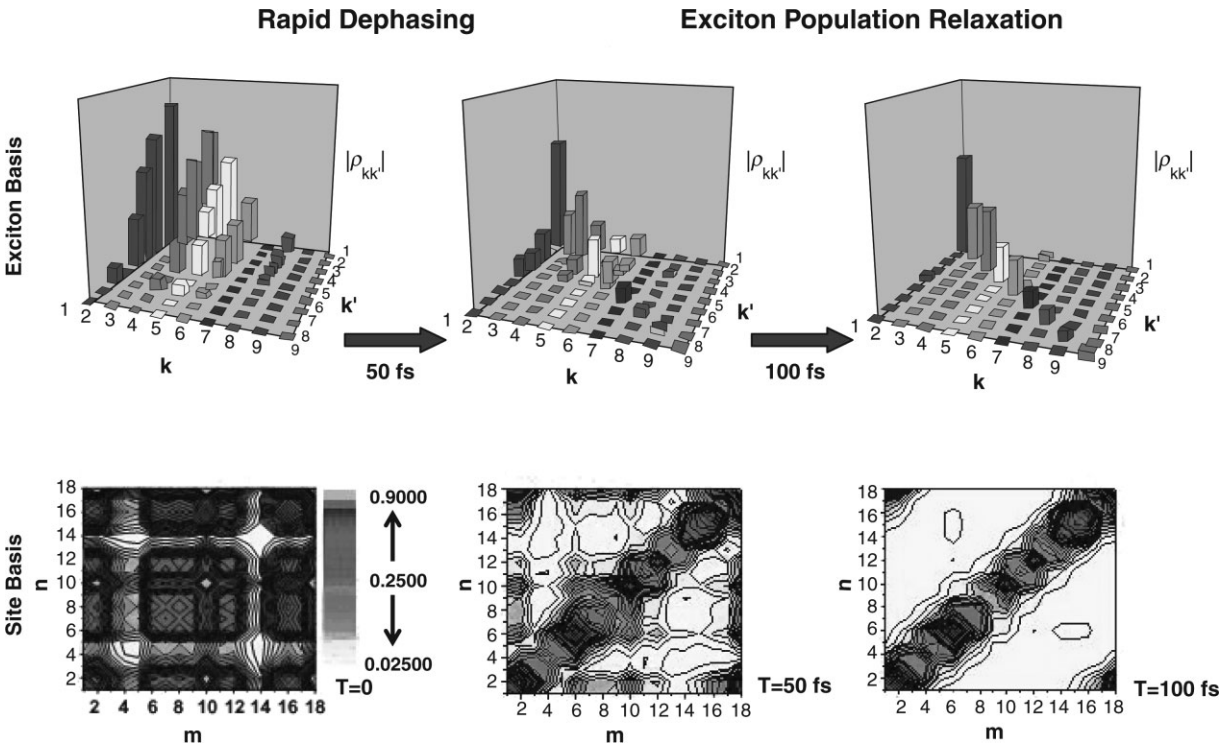

Figure 28. The density matrix as a function of time for a particular realization of the static disorder for the B850 band of LH2 in the exciton basis (*top panels*) and site basis (*bottom panels*). See text. Two nodes initially appear at the position of monomers with perpendicular transition dipole moments to the excitation laser polarization. See color insert.

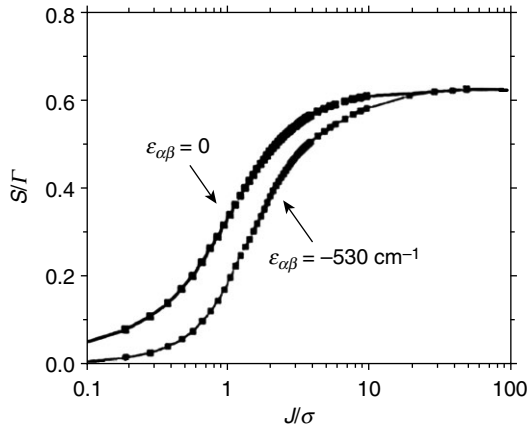

Figure 29. Ratio of exciton population relaxation rate (S) to the exciton pure dephasing rate (Γ) as a function of J/σ, where J is the electronic coupling and σ is the disorder. $\sigma = 150\,\mathrm{cm}^{-1}$ for B850 of LH2. The upper curve is for $\varepsilon_{\alpha\beta} = 0$, and the lower curve is for $\varepsilon_{\alpha\beta} = 550\,\mathrm{cm}^{-1}$. As S/Γ increases, energy transfer becomes more coherent.

"hopping" from one set of 2–4 molecules to an adjacent set of similar size. To what an extent is the hopping description justified. This can be quantified by considering the ratio of the hopping and dephasing rates. In the delocalized exciton picture, electron–phonon coupling is responsible for both the exciton hopping and dephasing processes. While the hopping rate between a pair of exciton states is proportional to spatial overlap of the states, the dephasing rate of an exciton state is proportional to the self-overlap of the spatial distribution of the state. Figure 29 shows the ratios of the two quantities as a function of J/s for a 18-Chl ring when s is fixed at $150\,\mathrm{cm}^{-1}$. For a given value of J/s, we take an average of the ratio over many realizations of static energies which determine spatial distributions of the partially delocalized exciton states. The black symbols are for the case when the mean energy of 18 Chls is identical, and the red symbols are the case when two Chls with an energy difference of $530\,\mathrm{cm}^{-1}$ are arrayed alternately. In both cases, the hopping rate is less than half of the dephasing rate when $J \leq 300\,\mathrm{cm}^{-1}$, which corresponds to the case of LH2. In other words, in the partially delocalized exciton picture, we can ignore coherence transfer, and the incoherent hopping process over the partially delocalized exciton states seems to be a reasonable description of the energy transfer dynamics in LH2.

F. Energy Transfer in PS-I

Figure 30 shows the results of global fits to the fluorescence decay of Photosystem I obtained by Kennis et al. [128] using the upconversion technique.

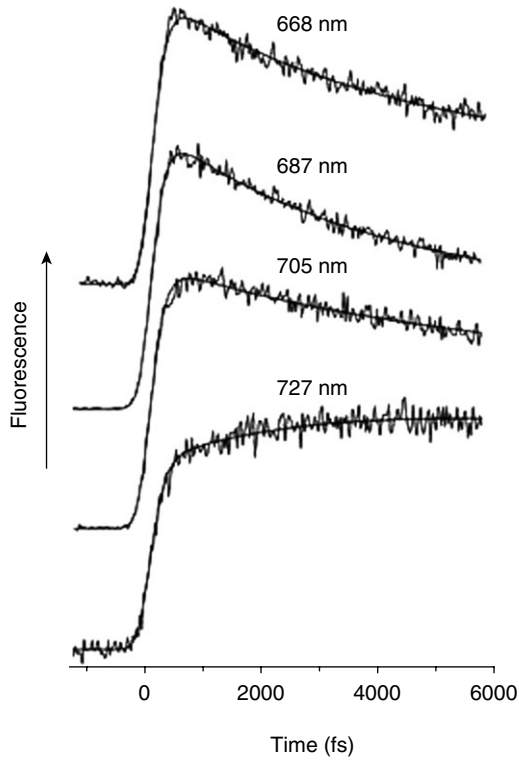

Figure 30. Fluorescence upconversion data from PS-I as a function of emission wavelength. Global fits to the data are also shown. See Ref. 139 for details.

The global fit of data recorded throughout the PSI fluorescence spectrum yielded four exponential components: 360 fs, 3.6 ps, 9.8 ps, and 38 ps. The longest time scale corresponds to the overall trapping time by the reaction center in PSI. A major difficulty of such fitting attempts is knowing whether the other time scales can be ascribed to specific physical processes or result from complex averages of microscopic time scales. In Ref. 128 the 360 fs was assigned to equilibration among Chla pigments in the bulk antenna, while the 3.6-ps component was associated with equilibration between bulk Chla and the red-shifted Chls, which seem unique to PSI. The 9.8 ps may relate to interactions between monomeric PSI units in the naturally occurring trimer.

Using calculated transition frequencies for all 96 Chls, spectral densities from experiment that reflect the inhomogeneity in electron–phonon coupling discussed in Section V.B, and the theoretical formalism described in Section VI.C, Yang et al. calculated the time scales of fluorescence decay in a PSI

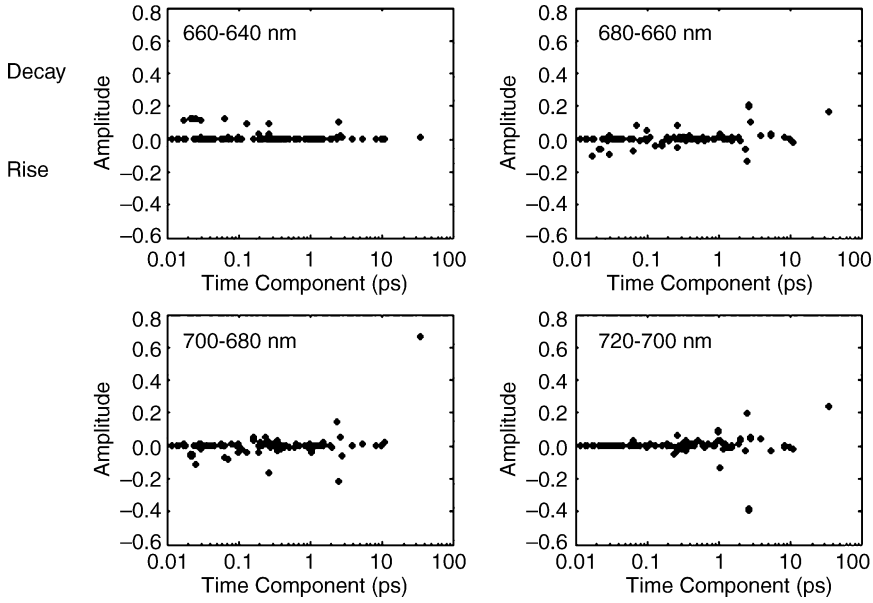

Figure 31. Calculated time scales of fluorescence decay in a PS-I monomer as a function of emission wavelength [97]. Excitation is at 640–660 nm, and the panels show the amplitudes of eigenvalues of the rate matrix for four different detection wavelengths. The amplitudes clearly cluster into four groups: <100 fs, $\sim$300 fs, 2–3 ps, and 38 ps, with the latter representing the overall trapping time.

monomer following excitation of a subset of Chls on the blue side of the spectrum (640–660 nm). Figure 31 shows the amplitudes and time scales (inverse of the rate matrix eigenvalue) for four different detection windows. Negative amplitudes correspond to a rising, and positive to a decaying, component. The plots in Fig. 31 reveal a small number of clusters of time constants which we divide into four groups: sub-100 fs, 0.3 ps, 2–3 ps, and 35–40 ps. Given that the fluorescence up-conversion study of Kennis et al. most likely did not have the time resolution to obtain the sub-100-fs components, the correspondence with the experimental data is striking. The 9.8-ps component does not appear strongly in the calculated result, suggesting that it is indeed associated with trimer formation.

Analysis of the decay associated spectra (DAS) with 10-nm resolution confirms the physical picture of the various time scales. The shortest time scales correspond to energy flow out of highest-energy Chls. The 0.3-ps component appears as a decay in the 650- to 670-nm windows and as a major rise at 680–700 nm (680 nm is the maximum of the absorption spectrum). The 2- to 3-ps

component appears as a rise only in the 690- to 710-nm window and corresponds to a steady flow of excitation from the blue to red via the 660- to 690-nm region during this time period. Finally, the 35- to 40-ps component is obtained as a major decay component at all wavelengths above 670 nm. This demonstrates that a steady state in the spectral distribution is reached before the longest time scale; in this steady state, excitation energy has been depleted in the blue region of the spectrum.

The remarkable consistency of the calculated and experimental time scales suggests that the calculations can be utilized to explore the microscopic details of the energy transfer processes. Such an analysis leads to the following conclusions:

1. The overall trapping time scale in PSI ($\sim$40 ps) has two main contributions: (a) Excitation energy diffusion in the antenna and transfer from the antenna to the RC Chls for the first time, which we refer to as the primary rate-determining step (RDS). This process contributes about 54% of the total time scale. (b) Subsequent processes that lead to the arrival of the excitation at P700 after the excitation has arrived at the RC. We call this the secondary RDS, and it includes energy transfer back to the antenna. The secondary RDS contributes the remaining 46% of the total trapping timescale, and it distinguishes PSI from the LHI/purple bacterial RC system where the equivalent of the primary RDS accounts for essentially the entire trapping time scale. This difference arises from (a) the energetic difference of the primary electron donor (P860) from the remaining RC components, which means that the antenna transfers only to the P860 and that P860 cannot transfer to the other RC components; (b) the lower dimensionality of the purple bacterial system; and (c) the absence of linker Chls in the bacterial system making the final step from LHI to P860 by far the slowest ($\sim$35 ps) in the overall trapping time scale of $\sim$50 ps.
2. Spectral equilibration occurs within the antenna in less than 5 ps and leads to a state characterized as a transfer equilibrium state, rather than a thermodynamic equilibrium state. By this we mean that single exponential fluorescence decay kinetics are observed at all detection wavelength on timescales longer than 5 ps.
3. As described in Section V.A, the energy configuration of the six RC Chls and two ''linker'' Chls is highly optimized for efficient trapping at P700 by forming a quasi-funnel structure.
4. The energy configuration of the remaining 88 Chls of PSI does not (at room temperature) influence the overall trapping time greatly. This arises from the high connectivity (dimensionality) of the PSI antenna, which mitigates against trapping of excitation on energetically unfavorable sites.

This makes the system very robust with respect to energetic disorder, again in contrast to the purple bacterial system which is quasi-one-dimensional.

5. The orientations of the antenna pigments (via their influence on the Coulombic couplings) do influence the efficiency of trapping to a moderate extent. The model suggests an electron transfer time scale in the range 0.87–1.7 ps from P700 to the primary electron acceptor, and this time scale does not have a strong influence on the overall trapping time scale.

VII PROTECTION AGAINST PHOTOCHEMICAL DAMAGE

Highly reactive, photo-oxidative species are inevitable byproducts of photosynthesis, and plants, cyanobacteria, and photosynthetic bacteria have evolved various mechanisms to deal with this problem. By far the most sophisticated mechanisms exist in green plants. An excess photon flux can exacerbate the damage caused by these intermediates, leading to problems ranging from reversible decreases in photosynthetic efficiency, to, in the worst case, death of the plant. Carotenoid molecules (Cars) constitute a key component of the protection system in all photosynthetic systems. In addition, carotenoids also act as light-harvesting pigments, providing spectral coverage between the Chl Q_y/Q_x and Soret bands. In some species, at least 95% of the excitation absorbed by the carotenoids is transferred to the B(Chls), while in other species significantly lower efficiencies are reported.

A crucial aspect of the photoprotective role of Cars is their ability to efficiently quench chlorophyll triplet states, thereby preventing the formation of excited, singlet oxygen by triplet–triplet energy transfer from its $^3\sum_g^-$ ground state:

$$\begin{aligned} {}^3\left({}^1Car\ {}^3Chl^*\right) &\rightarrow {}^3\left({}^3Car^*\ {}^1Chl\right) \\ {}^1\left({}^3O_2\ {}^3Chl^*\right) &\rightarrow {}^1\left({}^1O_2^*\ {}^1Chl\right) \end{aligned} \tag{36}$$

The mechanism of the efficient Chl-Car TT-EET has been investigated by Damjanovic et al. [129], but quantitatively accurate calculations of the electronic coupling have not yet been possible. Both triplet–triplet energy transfer and sensitization of singlet oxygen are mediated by interactions that depend on orbital overlap. Calculations are therefore highly sensitive to the accuracy of the wavefunctions. We note that a purely exchange-mediated interaction only operates when the wavefunctions are orthogonal and do not interpenetrate. The most significant orbital overlap-dependent coupling involves exchange of electrons by coupled, screened one-electron matrix elements [75, 130]. It is

straightforward to write down and compare the matrix elements corresponding to the EET processes of scheme (36), but this seems to be of limited practical use until it is possible to quantify such electronic couplings for realistic systems.

The mechanism of the efficient Chl-Car triplet–triplet transfer has been investigated by Damjanovic et al. [131], but quantitatively accurate calculations of the electronic couplings have yet not been possible.

In the singlet manifold, carotenoids have, like all polyenes, an unusual electronic structure: The first excited state (S_1) has the same symmetry, A_g^-, as the ground state, and thus one-photon transitions from S_0 to S_1 are forbidden. In other words, the S_1 state does not appear in the absorption (or emission) spectrum of carotenoids (with more than 9 double bonds), which is dominated by the very strong $S_0 \rightarrow S_2$ $\left(B_u^+\right)$ transition. Carotenoids also possess a state of B_u^- symmetry, which may lie near S_2, though evidence for the spectroscopic observation of this state remains controversial [132–135]. Finally, some unusual carotenoids with polar substituents, such as peridinin, may also have low-lying charge transfer states [42, 136, 137].

A decade ago it was considered that all carotenoid (B) Chl energy transfer was mediated through the S_1 state of the carotenoid because $S_2 \rightarrow S_1$ internal conversion would be too fast (100–200 fs) to allow significant transfer from S_2. More recently, it was concluded that a significant fraction, up to 100%, of the Car-Chl energy transfer does, in fact, take place from S_2. Although neither the Dexter nor Forster theories provide satisfactory predictions, we showed in Section III.D that Car S_1 states can have significant Coulombic coupling with Chl molecules despite the forbidden nature of the $S_0 \rightarrow S_1$ transition. Thus whether or not Car S_1 states play a role in energy transfer depends on the location of the S_1 state with respect to the (B) Chl Q_x and Q_y states. In the next section, we briefly describe recent experiments to determine the energies of S_1 states of photosynthetic carotenoids.

A. Carotenoids: Energy of the S_1 State

Two different methods have been used recently to determine the S_0–S_1 spectrum of carotenoids. Our group has utilized the two-photon allowed character of the S_0–S_1 transition to populate S_1, followed by subsequent detection of either S_1–S_n absorption or (B) Chl fluorescence resulting from S_1–Q_y energy transfer to determine the spectrum. Figure 32 shows both the energy level scheme and the excitation spectrum result for sphaeroidene, the carotenoid in the LH2 complex of *Rb. sphaeroides*. Note that the S_1 state lies in the region of negligible one-photon absorption between the strongly allowed B800/B850 (Q_y) bands and the Car S_0–S_2 band (Fig. 32). The fact that the S_1 lifetime of sphaeroidene is reduced from a solution value of 9 ps to 1.9 ps in LH2 is clear evidence for efficient $S_1 \rightarrow$ BChl energy transfer. In contrast, the S_1 state of rhodopin glucoside the carotenoid present in LH2 of *Rps. Acidophila* lies at too low an energy for

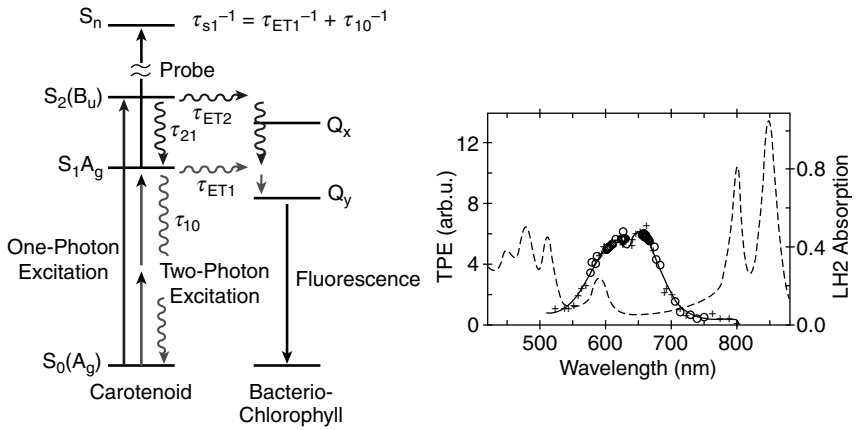

Figure 32. *Left*: Level scheme, excitation, and probing steps for carotenoid–chlorophyll interactions. *Right:* Two-photon excitation spectrum of sphaeroidene obtained by detecting fluorescence from Bchl in LH2 of *Rb. Sphaeroides*. See Ref. 156.

efficient $S_1 \rightarrow Q_y$ transfer and the S_1 lifetime in the complex is essentially unchanged from solution. Table V summarizes the energy transfer time constants and efficiencies for these two species. Such variations in the effectiveness of Car to Chl transfer seem quite common even for the same carotenoid in different contents. For example, the efficiency of β-carotene to Chla transfer is significantly higher in Photosystem I of plants and cyanobacteria than it is in the various light-harvesting complexes associated with Photosystem II in the same species [138–142].

The second method of obtaining the energy of the S_1 state was developed by Polivka, Zigmantis, Sundstrom and co-workers. It involves populating S_2 with an ultrashort laser pulse, allowing S_2–S_1 internal conversion to proceed and then scanning the S_1–S_2 absorption in their near-infrared [143]. The S_1 state energy is then obtained by subtraction. For reasons that are not entirely clear, the two-photon and near-IR probe methods do not always agree precisely on the S_1 state energies, although differences are quite small in most cases. For some

TABLE V
Calculated Car S_1–BChl Energy Transfer Time Constants and Efficiencies

Species	τ_{S1}/ps	τ_{ET1}/ps	ϕ_{ET1}	$\phi_{OA(9,11)}$	ϕ_{ET2}	$\phi_{ET1}\phi_{21}$	ϕ_{21}
Rb. sphaeroides	1.9 ± 0.5	2.4 ± 0.5	80%	>95%	>75%	<20%	<25%
Rps. acidophila	6.5 ± 0.5	>25	<28%	~70%	>60%	<10%	<40%

$\phi_{OA} = \phi_{ET2} + \phi_{ET1}\phi_{21}$

carotenoids, fluorescence and resonance Raman methods have been used to obtain S_0–S_1 energies, but these are extremely difficult to apply in intact photosynthetic complexes.

B. Regulation of Energy Transfer Efficiency

Photosystem II of plants [144] (specifically the D1 protein) is damaged sufficiently to require dismantling and repair in about 30 minutes in bright sunlight. To achieve even this degree of robustness, light harvesting in Photosystem II is highly regulated on both long and short time scales, by which in this context we mean hours versus minutes. The short-term regulation process is called *nonphotochemical quenching* (NPQ), which involves thermal dissipation of excitation energy-absorbed in PSII that exceeds a plant's capacity for CO_2 fixation [145]. Feedback de-excitation or energy-dependent quenching (qE) [146, 147] is the major rapidly reversible component of NPQ in a variety of plants. qE is characterized by a light-induced absorbance change at 535 nm [148], the shortening of the overall chlorophyll fluorescence lifetime (or equivalent reduction in fluorescence yield) [149]. It requires the buildup of a pH gradient across the thylakoid membrane, under conditions of excess light. The pH gradient, in turn, triggers the enzymatic conversion of the carotenoid vioaxanthin (Vio) to zeaxanthin (Zea) via the xanthophylls cycle [150]. In addition, the presence of a specific pigment-binding protein, Psbs (CP22) is essential for *qE* [151].

Currently, two hypotheses concerning the mechanism of *qE* exist, one in which the effect of Zea is solely structural (called *indirect quenching*) and the other in which Zea acts as an energy acceptor for excitation transfer from the Chl Q_y state (called *direct quenching*). Clearly, the direct quenching mechanism depends strongly on the relative Q_y–S_1 energies levels of the Chl and Car molecules. Using the near-IR probing method, Polivka et al. found that in solution both Vio and Zea S_1 states lie below the Chl Q_y energy and could both act as quenchers in principle, although Vio does not [143]. Very recently, Ma et al. [152] found strong evidence for the formation of the Zea S_1 state following Chl excitation, only under conditions of maximum *qE*. This result appears to strongly support the direct quenching mechanism, but much remains to be clarified before a molecular mechanism for NPQ is at hand.

VIII. SUMMARY AND CONCLUSIONS

Early studies—for example, the work of Arnold and co-workers [153, 154] and Duysens [155]—exposed the role of energy transfer in the capture of light by chlorophyll pigments and subsequent transfer to a trap. Such studies were considerably aided by Förster theory, which provided a means to predict energy transfer rates based on simple experimental observables.

In recent years, ultrafast spectroscopies revealed the most rapid energy transfer events in photosynthetic proteins, which could not be readily explained by predictions from Förster theory. As high-resolution structural models became available and more realistic models for light harvesting were explored, it became clear that conventional Förster theory was missing some essential element of the problem. A number of possibilities were discussed, including the possibility that orbital overlap effects were important. Finally, we realized that (i) we needed to think about molecular aggregates differently than molecular pairs—we needed to retain structural information in the model for EET as in the GFT model; (ii) we had to learn how to calculate Coulombic couplings between molecules which led to the development of the TDC method; (iii) we needed to incorporate such ideas into dynamical models for large, complex aggregates in order to simulate various ultrafast spectroscopies, including photon echoes.

At this point, we can suggest some open questions:

1. *The Exact Nature of the Protein as a Phonon Bath and Dielectric Environment*. At this point there exists no satisfactory quantitative description of dielectric screening and local field effects in energy transfer, except in the limit of large donor–acceptor separations (the $1/n^4$ factor). This appears to be an important point to resolve, since the effect on the rate can amount to a factor of ~ 4. A particular challenge will be to calculate or measure medium effects in a protein as opposed to a dielectric continuum.
2. *The Time Scales and Mechanism of "Quasi-coherent" Excitation Hopping Within B850/B875 Rings*. This appears to be an area where simple theory cannot apply. It will be a challenge for experimentalists and theorists to address this issue collaboratively. For example, it is not clear whether linear coupling to a harmonic bath is adequate to describe such systems. For example, it may be necessary to include multiphonon and Duschinsky effects on the dynamics in order to describe the influence of temperature on such systems.
3. *The Signatures of Interactions Between Carotenoids and Chlorophylls in Ultrafast Experiments*. These interactions are not well-characterized at present. The influence of orbital mixing [156] and the potential formation of low-lying charge transfer states between carotenoid and chlorophyll molecules [157] should be detectable spectroscopically. An understanding of these interactions will help to elucidate the role of carotenoids in mediating long-range Chl–Chl energy transfer and in the poorly understood phenomenon of nonphotochemical quenching described in Section VII.B.
4. *The Mechanism of Energy Flow in Photosystem II*. Partly because of the lack of atomic-level structural information and partly because the energy

landscape of Photosystem II is nearly flat, giving no time-scale separation between energy and electron transfer dynamics, the overall energy flow within the Photosystem II supercomplex is not understood in detail. Because of the size and complexity of the entire system—in particular, the need to incorporate regulatory systems—some kind of coarse-graining will almost certainly be necessary. Yang and Fleming [158] have developed a ''domain'' model that enables the identification of bottlenecks and key time scales in any disordered antenna system. The model requires a rate matrix for the system, but given this, the method provides a systematic way to define compartment models of the type often used intuitively to describe energy transfer in multicomponent systems. Energy flow in PSII will require modeling of EET between pigment–protein complexes. Here questions of excitation delocalization become critical since they define ''short''- and ''long''-range interactions. It will be interesting to ascertain the role, if any, of molecular aggregates (i.e., Generalized Forster Theory) in this process.

5. *The Experimental Characterization of Spatially and Energetically Disordered (in Both the Diagonal and Off-Diagonal Senses) Energy Transfer Systems*. Despite the great advances in ultrafast spectroscopy, characterizing multicomponent systems where both electronic and electron–phonon couplings are distributed remains a challenge. Multidimensional spectroscopy [159]—in particular, the two-color photon echo [160]—holds promise for significantly more incisive studies of such systems, but considerable development work, both experimentally and theoretically, remains to be done.

Acknowledgments

The work at Berkeley was supported in its entirety by the Director, Office of Science, Office of Basic Energy Sciences, Chemical Sciences Division, of the U.S. Department of Energy under Contract DE-AC03-76SF00098. We are grateful to Dr. Mary Gress for her support of our work. The ideas and results described here represent contributions from many colleagues and co-workers. Our debt to the following people is great: Brent Krueger, Peter Walla, Chao-Ping (Cherri) Hsu, Jenny Yom, Xanthipe Jordanides, Ana Damjanovic, Harsha Vaswani, Nancy Holt, Ying-Zhong Ma, Patricia Linden, John Kennis, Ritesh Agarwal, Bradley Prall, Abbas Rizvi, Mino Yang, Martin Head-Gordon, Petra Fromme, Krishna Niyogi, and Jeffrey Reimers.

References

1. C.-P. Hsu, P. J. Walla, M. Head-Martin, and G. R. Fleming, *J. Phys. Chem. B* **105**, 11016 (2001).
2. R. v. Grondelle, J. P. Dekker, T. Gillbro, and V. Sundstrom, *Biochim. Biophys. Acta* **1187**, 1 (1994).
3. G. R. Fleming, S. A. Passino, and Y. Nagasawa, *Philos. Trans. R. Soc. London A* **356**, 389 (1998).
4. D. L. Dexter, *J. Chem. Phys.* **21**, 836 (1953).

5. G. R. Fleming and R. von Grondelle, *Curr. Opin. Struct. Biol.* **7**, 738 (1997).
6. T. Pullerits and V. Sundstrom, *Acc.Chem. Res.* **29**, 381 (1996).
7. V. Sundstrom, T. Pullerits, and R. von Grondelle, *J. Phys. Chem. B* **103**, 2327 (1998).
8. X. Hu, A. Damjanovic, T. Ritz, and K. Schulten, *Proc. Natl. Acad. Sci. USA* **95**, 5935 (1998).
9. R. G. Alden, E. Johnson, V. Nagarajan, W. W. Parson, C. J. Law, and R. G. Cogdell, *J. Phys. Chem. B* **101**, 4667 (1997).
10. R. Jimenez, S. N. Dikshit, S. E. Bradforth, and G. R. Fleming, **100**, 6825 (1996).
11. S. Tretiak, C. Middleton, V. Chernyak, and S. Mukamel, *J. Phys. Chem. B* **104**, 9540 (2000).
12. W. W. Parson and A. Warshel, *J. Am. Chem. Soc.* **109**, 6152 (1986).
13. Y. Won and R. A. Friesner, *J. Phys. Chem.* **92**, 2208 (1988).
14. E. J. P. Lathrop and R. A. Friesner, *J. Phys. Chem.* **98**, 3056 (1994).
15. M. A. Thompson and M. C. Zerner, *J. Am. Chem. Soc.* **113**, 8210 (1991).
16. G. D. Scholes and G. R. Fleming, *J. Phys. Chem. B* **104**, 1854 (2000).
17. X. J. Jordanides, G. D. Scholes, and G. R. Fleming, *J Phys. Chem. B* **105**, 1652 (2001).
18. G. McDermott, S. M. Prince, A. A. Freer, A. M. Hawthornthwaite-Lawless, M. Z. Papiz, and R. J. Cogdell, *Nature* **374**, 517 (1995).
19. S. Karrasch, P. Bullough, and R. Ghosh, *EMBOJ* **14**, 631 (1995).
20. A. Freer, S. Prince, K. Sauer, M. Papiz, A. Hawthornthwaite-Lawless, G. McDermott, R. Cogdell, and N. W. Isaacs, *Structure* **4**, 449 (1996).
21. J. Koepke, X. Hu, C. Muenke, K. Schulten, and H. Michel, *Structure* **4**, 581 (1996).
22. X. Hu, T. Ritz, A. Damjanovic, and K. Schulten, *J. Phys. Chem. B* **101**, 3854 (1997).
23. X. Hu and K. Schulten, *Biophys. J.* **75**, 683 (1998).
24. K. J. Visscher, H. Bergstrom, V. Sundstrom, C. N. Hunter, and R. von Grondelle, *Photosynth. Res.* **3**, 211 (1989).
25. H. Bergstrom, R. von Grondelle, and V. Sundstrom, *FEBS Lett.* **2**, 503 (1989).
26. A. Freiberg, J. P. Allen, J. C. Williams, and N. W. Woodbury, *Photosynth. Res.* **1–2**, 309 (1996).
27. T. Pullerits, K. J. Visscher, S. Hess, V. Sundstrom, A. Freiberg, K. Timpmann, and R. von Grondelle, *Biophys. J.* **66**, 236 (1994).
28. S. Hess, M. Chachisvilis, K. Timpmann, M. R. Jones, G. J. S. Fowler, C. N. Hunter, and V. Sundstrom, *Proc. Natl. Acad. Sci. USA* **26**, 12333 (1995).
29. V. Nagarajan and W. W. Parson, *Biochemistry* **36**, 2300 (1997).
30. H. Bergstrom, V. Sundstrom, R. von Grondelle, T. Gillbro, and R. Cogdell, *Biochim. Biophys. Acta* **936**, 90 (1988).
31. Y.-Z. Ma, R. J. Cogdell, and T. Gillbro, *J Phys. Chem. B* **101**, 1087 (1997).
32. J. T. M. Kennis, A. M. Streltsov, T. J. Aartsma, T. Nozawa, and J. Amesz, *J. Phys. Chem.* **100**, 2438 (1996).
33. T. Pullerits, S. Hess, J. L. Herek, and V. Sundstrom, *J Phys. Chem. B* **101**, 10560 (1997).
34. A. P. Shreve, J. K. Trautman, H. A. Frank, T. G. Owens, and A. C. Albrecht, *Biochim. Biophys. Acta* **1058**, 280 (1991).
35. S. Hess, F. Feldchtein, A. Babin, I. Nurgaleev, T. Pullerits, A. Sergeev, and V. Sundstrom, *Chem. Phys. Lett.* **216**, 247 (1993).
36. H. J. Kramer, R. V. Grondelle, C. N. Hunter, W. H. J. Westerhaus, and J. Amesz, *Biochim. Biophys. Acta* **765**, 156 (1984).

37. J. M. Salverda, F. von Mourik, G. van der Zwan, and R. von Grondelle, *J Phys. Chem. B* **104** (2000).
38. R. Agarwal, M. Yang, Q.-H. Xu, and G. R. Fleming, *J Phys. Chem. B* **105**, 1187 (2001).
39. H. A. Frank and R. J. Cogdell, *Photochem. Photobiol.* **63**, 257 (1996).
40. M. Yang, R. Agarwal, and G. R. Fleming, *Photochem. Photobiol. Part A* **142**, 107 (2001).
41. Y. Koyama, M. Kuki, P.-O. Andersson, and T. Gillbro, *Photochem. Photobiol.* **63**, 243 (1996).
42. D. Zigmantas, R. G. Hiller, V. Sundstrom, and T. Polivka, *Proc. Natl. Acad. Sci. USA* **99**, 16760 (2002).
43. J. Breton, J.-L. Martin, A. Migus, A. Antonetti, and A. Orszag, *Proc. Natl. Acad. Sci. USA* **83**, 5121 (1986).
44. J. Breton, J.-L. Martin, G. R. Fleming, and J.-C. Lambry, *Biochemistry* **27**, 8276 (1988).
45. Y. W. Jia, D. M. Jonas, T. H. Joo, Y. Nagasawa, M. J. Lang, and G. R. Fleming, *J. Phys. Chem.* **99**, 6263 (1995).
46. D. M. Jonas, M. J. Lang, Y. Nagasawa, S. E. Bradforth, S. N. Dikshit, R. Jiminez, T. Joo, and G. R. Fleming, in *Proceedings of the Feldafing III Workshop, Munich* (1995).
47. R. J. Stanley, B. King, and S. G. Boxer, *J. Phys. Chem.* **100**, 12052 (1996).
48. S. Lin, A. K. W. Taguchi, and N. W. Woodbury, *J. Phys. Chem.* **100**, 17067 (1996).
49. G. Haran, K. Wynne, C. C. Moser, P. L. Dutton, and R. M. Hochstrasser, *J. Phys. Chem.* **100**, 5562 (1996).
50. M. H. Vos, J. Breton, and J. L. Martin, *J. Phys. Chem. B* **101**, 9820 (1997).
51. B. A. King, R. J. Stanley, and S. G. Boxer, *J. Phys. Chem. B* **101**, 3644 (1997).
52. S. I. E. Vulto, A. M. Streltsov, A. Y. Shkuropatov, V. A. Shuvalov, and T. J. Aartsma, *J. Phys. Chem. B* **101**, 7249 (1997).
53. D. C. Arnett, C. C. Moser, P. L. Dutton, and N. F. Scherer, *J. Phys. Chem. B* **103**, 2014 (1999).
54. B. A. King, T. McAnaney, A. deWinter, and S. G. Boxer, *J. Phys. Chem. B* **104**, 8895 (2000).
55. H. Michel, *J. Mol. Biol.* **158**, 567 (1982).
56. J. Deisenhofer, O. Epp, I. Sinning, and H. Michel, *J. Mol. Biol.* **246**, 429 (1995).
57. C. H. Chang, O. Elkabbani, D. Tiede, J. Norris, and M. Schiffer, *Biochemistry* **30**, 5352 (1991).
58. U. Ermler, G. Fritzsch, S. K. Buchanan, and H. Michel, *Structure* **2**, 925 (1994).
59. L. Slooten, *Biophys. Biochim. Acta* **256**, 452 (1972).
60. T. Förster, *Ann. Phys.* **6**, 55 (1948).
61. S. Mukamel, *Principles of Nonlinear Optical Spectroscopy*, Oxford University Press, New York, 1995.
62. B. W. van der Meer, G. I. Coker, and S.-Y. Chen, *Resonance Energy Transfer, Theory and Data*, VCH Publishers, New York, 1994.
63. G. D. Scholes, X. J. Jordanides, and G. R. Fleming, *J. Phys. Chem. B.* **105**, 1640 (2001).
64. G. D. Scholes, *Annu. Rev. Phys. Chem.* **54**, 57 (2003).
65. G. J. S. Fowler, W. Crielaard, R. W. Visschers, R. von Grondelle, and C. N. Hunter, *Photochem. Photobiol.* **57**, 2 (1993).
66. A. Gall, G. J. S. Fowler, C. N. Hunter, and B. Robert, *Photochem. Photobiol.* **36**, 16282 (1997).
67. G. J. S. Fowler, R. W. Visschers, G. G. Grief, R. von Grondelle, and C. N. Hunter, *Nature* **355**, 848 (1992).
68. R. K. and R. M. Hochstrasser, *J Chem. Phys.* **109**, 855 (1998).
69. T. P. and A. Freiberg, *Chem. Phys.* **149**, 409 (1991).

70. M. Beauregard, I. Martin, and A. R. Holzwarth, *Biochim. Biophys. Acta* **1060**, 271 (1991).
71. S. Hess, E. Akesson, R. J. Cogdell, T. Pullerits, and V. Sundstrom, *Biophys. J.* **69**, 2211 (1995).
72. S. Jang, S. E. Dempster, and R. J. Silbey, *J Phys. Chem. B* **105**, 6655 (2001).
73. B. P. Krueger, G. D. Scholes, and G. R. Fleming, *J. Phys. Chem. B* **102**, 5378 (1998).
74. G. D. Scholes, I. R. Gould, R. J. Cogdell, and G. R. Fleming, *Phys. Chem. B* **103**, 2543 (1999).
75. G. D. Scholes and K. P. Ghiggino, *J. Phys. Chem.* **98**, 4580 (1994).
76. R. McWeeny, *Methods of Molecular Quantum Mechanics*, 2nd ed., Academic Press, London, 1992.
77. G. D. Scholes, R. D. Harcourt, and G. R. Fleming, *J. Phys. Chem. B* **101**, 7302 (1997).
78. D. P. Craig and T. Thirunamachandran, *Molecular Quantum Electrodynamics*, Academic Press, New York, 1984.
79. R. J. Buehler and J. O. Hirschfelder, *Phys. Rev.* **83**, 628 (1951).
80. A. D. Buckingham, *Intermolecular Forces—From Diatomics to Biopolymers*, Wiley, New York, 1978.
81. F. London, *J. Phys. Chem.* **46**, 305 (1942).
82. D. Beljonne, G. Pourtois, C. Silva, E. Hennebicq, L. M. Herz, R. H. Friend, G. D. Scholes, S. Setayesh, K. Mullen, and J. L. Bredas, *Proc. Natl. Acad. Sci. USA* **99**, 10982 (2002).
83. P. J. Walla, P. A. Linden, C.-P. Hsu, G. D. Scholes, and G. R. Fleming, *Proc. Natl. Acad. Sci. USA* **97**, 10808 (2000).
84. R. Mulliken, *J. Chem. Phys.* **23**, 1833 (1955).
85. R. Mulliken, *J. Chem. Phys.* **23**, 2343 (1955).
86. S. Tretiak and S. Mukamel, *Chem. Rev.* **102**, 3171 (2002).
87. S. Mukamel, S. Tretiak, T. Wagersreiter, and V. Chernyak, *Science* **277**, 781 (1997).
88. A. J. Hoff and J. Deinsenhofer, *Phys. Rep.* **287**, 1 (1997).
89. C. A. Wraight and R. K. Clayton, *Biochim. Biophys. Acta* **333**, 246 (1974).
90. R. K. Clayton, *Photochem. Photobiol.* **1**, 201 (1962).
91. J. A. Jackson, S. Lin, A. K. W. Taguchi, J. C. Williams, J. P. Allen, and N. W. Woodbury, *J. Phys. Chem. B* **101**, 5747 (1997).
92. X. Jordanides, G. D. Scholes, W. A. Shapley, J. R. Remers, and G. R. Fleming, *J. Phys. Chem. B* **108**, 1753 (2004).
93. J. R. Reimers and N. S. Hush, *J. Am. Chem. Soc.* **117**, 1302 (1995).
94. R. S. Knox and H. von Amerongen, *J Phys. Chem. B* **106**, 5289 (2002).
95. J. D. Dow, *Phys. Rev.* **174**, 962 (1968).
96. C.-P. Hsu, M. Head-Gordon, T. Head-Gordon, and G. R. Fleming, *J. Chem. Phys.* **114**, 3065 (2001).
97. M. Yang, A. Damjanovic, H. Vaswani, and G. R. Fleming, *Biophys. J.* **85**, 1 (2003).
98. R. Agarwal, A. H. Rizvi, B. S. Prall, J. D. Olsen, C. N. Hunter, and G. R. Fleming, *J. Phys. Chem. A.* **106**, 7573 (2002).
99. A. Damjanovic, H. M. Vaswani, P. Fromme, and G. R. Fleming, *J. Phys. Chem. B.* **106**, 10251 (2002).
100. V. Zazubovich, S. Matsuzuki, T. W. Johnson, J. M. Hayes, P. R. Chitnis, and G. J. Small, *Chem. Phys.* **275**, 47 (2002).
101. I. R. Mercer, I. R. Gould, and D. R. Klug, *J. Phys. Chem. B.* **103**, 7720 (1999).
102. G. Zucchelli, R. C. Jennings, F. M. Garlaschi, G. Cinque, R. Bassi, and O. Cremonesi, *Biophysical Journal* **82**, 378 (2002).

103. T. Pullerits and A. Freiberg, *Chem. Phys.* **149**, 409 (1991).
104. T. Pullerits and A. Freiberg, *Biophys. J.* **63**, 879 (1992).
105. S. E. Bradforth, R. Jimenez, F. von Mourik, R. von Grondelle, and G. R. Fleming, *J. Phys. Chem.* **99**, 16179 (1995).
106. J. M. Jean, C. K. Chan, and G. R. Fleming, *Isr. J. Chem.* **28**, 169 (1988).
107. R. Agarwal, B. P. Krueger, G. D. Scholes, M. Yang, J. Yom, L. Mets, and G. R. Fleming, *J. Phys. Chem. B* **104**, 2908 (2000).
108. O. Kuhn and V. Sundstrom, *J Chem. Phys.* **107**, 4154 (1997).
109. A. G. Redfield, *Adv. Magn. Reson.* **1**, 1 (1965).
110. W. T. Pollard, A. K. Felts, and R. A. Friesner, *Adv. Chem. Phys.* **93**, 77 (1996).
111. J. M. Jean, R. A. Friesner, and G. R. Fleming, *J Chem. Phys.* **96**, 5827 (1992).
112. J. M. Jean and G. R. Fleming, *J Chem. Phys.* **103**, 2092 (1995).
113. A. K. Felts, W. T. Pollard, and R. A. Friesner, *J. Phys. Chem.* **99**, 2929 (1995).
114. M. Morillo, C. Denk, and R. I. Cukier, *Chem. Phys.* **212**, 157 (1996).
115. J. M. Jean, *J. Chem. Phys.* **104**, 5638 (1996).
116. J. M. Jean, *J. Phys. Chem. A* **102**, 7549 (1998).
117. C. F. Jen and A. Warshel, *J. Phys. Chem. A* **103**, 11378 (1999).
118. P. Herman and I. Barvik, *J. Phys. Chem. B* **103**, 10892 (1999).
119. P. Herman and I. Barvik, *J. Lumin.* **83-84**, 247 (1999).
120. D. Kilin, U. Kleinekathofer, and M. Schreiber, *J. Phys. Chem. A* **104** (2000).
121. M. Yang and G. R. Fleming, *Chem. Phys.* **282**, 161 (2002).
122. J. L. Herek, N. J. Fraser, T. Pullerits, P. Martinsson, T. Polivka, H. Scheer, R. J. Cogdell, and V. Sundstrom, *Biophys. J.* **78**, 2590 (2000).
123. E. W. Knapp, *Chem. Phys.* **85**, 73 (1984).
124. K. Ohta, M. Yang, and G. R. Fleming, *Chem. Phys.* **115**, 7609 (2001).
125. H. B. Thacker, *Rev. Mod. Physics* **53**, 253 (1981).
126. M. Wubs and J. Knoester, *Chem. Phys. Lett.* **284**, 63 (1998).
127. L. D. Bakalis, M. Coca, and J. Knoester, *J. Chem. Phys.* **110**, 2208 (1999).
128. J. T. M. Kennis, B. Gobets, I. H. M. von Stokkum, J. P. Dekker, R. von Grondelle, and G. R. Fleming, *J. Phys. Chem.* **105**, 4485 (2001).
129. A. Damjanovic, I. Kosztin, U. Kleinekathoefer, and K. Schulten, *Phys. Rev. E.* **65**, 031919 (2002).
130. G. D. Scholes, R. D. Harcourt, and K. P. Ghiggino, *J. Chem. Phys.* **101**, 10521 (1994).
131. A. Damjanovic, T. Ritz, and K. Schulten, *Phys. Rev.* **59**, 3293 (1999).
132. T. Sashima, H. Nagae, M. Kuki, and Y. Koyama, *Chem. Phys. Lett.* **299**, 187 (1999).
133. T. Sashima, Y. Koyama, T. Yamada, and H. Hashimoto, *J. Phys. Chem. B* **104**, 5011 (2000).
134. M. Yoshizawa, H. Aoki, and H. Hashimoto, *Phys. Rev. B* **63**, 180301 (2001).
135. G. Cerullo, D. Polli, G. Lanzani, S. D. Silvestri, H. Hashimoto, and R. J. Cogdell, *Science* **298**, 2395 (2002).
136. D. Zigmantas, T. Polivka, R. G. Hiller, A. Yartsev, and V. Sundstrom, *J. Phys. Chem. A.* **105**, 10296 (2001).
137. J. A. Bautista, R. E. Connors, B. B. Raju, R. G. Hiller, F. P. Sharples, D. Gosztola, M. R. Wasielewski, and H. A. Frank, *J. Phys. Chem. B* **103**, 8751 (1999).

138. J. T. M. Kennis, *Unpublished results.*

139. B. Gobets, J. T. M. Kennis, J. A. Ihalainen, M. Brazzoli, R. Croce, I. H. M. von Stokkum, R. Bassi, J. P. Dekker, H. von Amerongen, G. R. Fleming, and R. von Grondelle, *J. Phys. Chem. B* **105**, 10132 (2001).

140. J. van der Lee, D. Bald, S. L. S. Kwa, R. von Grondelle, M. Rogner, and J. P. Dekker, *Photosynth. Res.* **34**, 311 (1993).

141. F. L. der Weerd, I. H. M. von Stokkum, H. von Amerongen, J. P. Dekker, and R. von Grondelle, *Biophys. J.* **82**, 1586 (2002).

142. R. J. Vandorssen, J. Breton, and J. J. P. et al., *Biochim. Biophys. Acta* **893**, 267 (1987).

143. T. Polivka, J. L. Herek, D. Zigmantas, H.-E. Akerlund, and V. Sundstrom, *P. Natl. Acad. Sci. USA* **96**, 4914 (1999).

144. B. Andersson, A. H. Salter, I. Virgin, I. Vass, and S. Styring, *J. Photochem. Photobiol. B* **15**, 15 (1992).

145. K. K. Niyogi, *Annu. Rev. Plant Phys.* **50**, 333 (1999).

146. P. Horton, A. V. Ruban, and R. G. Walters, *Annu. Rev. Plant Phys.* **47**, 655 (1996).

147. P. Muller, X. P. Li, and K. K. Niyogi, *Plant Physiol.* **125**, 1558 (2001).

148. A. M. Gilmore, *Physiol. Plant.* **99**, 197 (1997).

149. A. M. Gilmore, T. L. Hazlett, and Govindjee, *Proc. Natl. Acad. Sci. USA* **92**, 2273 (1995).

150. A. M. Gilmore and H. Y. Yamamoto, *P. Natl. Acad. Sci. USA* **5**, 1899 (1992).

151. X. P. Li, O. Bjorkman, and C. Shih, *Nature* **403**, 391 (2000).

152. Y.-Z. Ma, N. E. Holt, X. P. Li, K. K. Niyogi, and G. R. Fleming, *Proc. Natl. Acad. Sci. USA* **100**, 4377 (2003).

153. R. Emerson and W. Arnold, *J. Gen. Physiol.* **16**, 191 (1932).

154. W. Arnold and J. K. Oppenheimer, *J. Gen. Physiol.* **33**, 423 (1949).

155. L. N. M. Duysens, *Thesis. Leiden.* 1952.

156. B. P. Krueger, J. Yom, P. J. Walla, and G. R. Fleming, *Chem. Phys. Lett.* **310**, 57 (1999).

157. A. Dreuw, G. R. Fleming, and M. Head-Gordon, *Phys. Chem. Chem. Phys.* **5**, 3247 (2003).

158. M. Yang and G. R. Fleming, *J. Chem. Phys.* **119**, 5614 (2003).

159. H. M. Vaswani, C.-P. Hsu, M. Head-Gordon, and G. R. Fleming, *J. Phys. Chem. B* **107**, 7940 (2003).

160. R. Agarwal, B. S. Prall, A. H. Rizvi, M. Yang, and G. R. Fleming, *J Chem. Phys.* **116**, 6243 (2002).

161. L. J. Kaufman, D. A. Blank, and G. R. Fleming, *J. Chem. Phys.* **114**, 2312 (2001).

162. P. Jordan, P. Fromme, H. T. Witt, O. Klukas, W. Saenger, and N. Krauss, *Nature* **411**, 909 (2001).

163. M. Yang and G. R. Fleming, *Chem. Phys.* **282**, 161 (2002).